


Accurate Electronic Properties and Intercalation Voltages of Olivine-Type Li-Ion Cathode Materials from Extended Hubbard Functionals

Iurii Timrov^{1,*}, Francesco Aquilante,¹ Matteo Cococcioni², and Nicola Marzari^{1,3}

¹Theory and Simulation of Materials (THEOS), and National Centre for Computational Design and Discovery of Novel Materials (MARVEL), École Polytechnique Fédérale de Lausanne (EPFL), Lausanne CH-1015, Switzerland

²Department of Physics, University of Pavia, via Bassi 6, Pavia I-27100, Italy

³Laboratory for Materials Simulations, Paul Scherrer Institut, Villigen PSI 5232, Switzerland

 (Received 7 April 2022; revised 26 September 2022; accepted 4 October 2022; published 31 October 2022)

The design of novel cathode materials for Li-ion batteries would greatly benefit from accurate first-principles predictions of structural, electronic, and magnetic properties as well as intercalation voltages in compounds containing transition-metal elements. For such systems, density-functional theory (DFT) with standard (semi)local exchange-correlation functionals is of limited use as it often fails due to strong self-interaction errors that are especially relevant in the partially filled d shells. Here, we perform a detailed comparative study of the phospho-olivine cathode materials Li_xMnPO_4 , Li_xFePO_4 and the mixed transition metal $\text{Li}_x\text{Mn}_{1/2}\text{Fe}_{1/2}\text{PO}_4$ ($x = 0, 1/4, 1/2, 3/4, 1$) using four electronic-structure methods: DFT, DFT+ U , DFT+ $U+V$, and HSE06. We show that DFT+ $U+V$, with onsite U and intersite V Hubbard parameters determined from first principles and self-consistently with respect to the structural parameters by means of density-functional perturbation theory (linear response), provides the most accurate description of the electronic structure of these challenging compounds. In particular, we demonstrate that DFT+ $U+V$ displays very clearly “digital” changes in oxidation states of the transition-metal ions in all compounds, including the mixed-valence phases occurring at intermediate Li concentrations, leading to voltages in remarkable agreement with experiments. We show that the inclusion of intersite Hubbard interactions is essential for the accurate prediction of thermodynamic quantities, balancing the drive for localization induced by the onsite U with intersite V orbital hybridizations. At variance with other methods, DFT+ $U+V$ describes accurately such localization-hybridization interplay, and thus opens the door for the study of more complex cathode materials as well as for a reliable exploration of the chemical space of compounds for Li-ion batteries.

DOI: [10.1103/PRXEnergy.1.033003](https://doi.org/10.1103/PRXEnergy.1.033003)

I. INTRODUCTION

Recent years have witnessed urgent needs for renewable energy and the availability of energy storage technology that is needed at all scales. One of the major advances in this area can be traced back to the development of Li-ion rechargeable batteries [1,2] that are currently employed in a variety of applications, e.g., for portable electronics, power tools, automotive industry, electricity grids, to name a few [3,4]. These technologies are in increasing demand due to a global increase in energy consumption

and a widening dependence on the availability of efficient, safe, and nontoxic Li-ion batteries.

The properties and performance of Li-ion batteries (such as power and energy density, capacity retention, cyclability, thermal stability, etc.) depend on many factors and their interplay within the complexity of the actual multicomponent devices. As part of this network, cathode materials play a pivotal role, determining the Li intercalation voltage and cyclability of Li^+ ions through the interface with the electrolyte. There are various types of cathode materials, among which we mention layered, spinel, olivine, prussian blue, and cation-disordered rock-salt [5–7]. A key ingredient of cathodes are transition-metal (TM) elements that are electrochemically active species that change their oxidation state during charging and discharging of the battery. It is therefore of paramount importance to understand at the atomistic level what properties of such compounds lead to efficient electrochemical processes.

*iurii.timrov@epfl.ch

Published by the American Physical Society under the terms of the [Creative Commons Attribution 4.0 International](https://creativecommons.org/licenses/by/4.0/) license. Further distribution of this work must maintain attribution to the author(s) and the published article's title, journal citation, and DOI.

An important tool for studying cathode materials is density-functional theory (DFT) [8,9], which is a workhorse for first-principles simulations in physics, chemistry, and materials science. DFT requires approximations to the exchange-correlation (XC) functional, with local spin-density approximation (LSDA) and spin-polarized generalized-gradient approximation (σ -GGA) being the most popular ones. However, these approximations often provide some unsatisfactory results (e.g., voltages, formation energies, change in the atomic occupations in mixed-valence compounds, etc.) for many TM compounds due to self-interaction errors (SIEs) [10,11] that are especially large for localized d and f electrons. For this reason, more accurate approaches beyond “standard DFT” (i.e., based on LSDA or σ -GGA) are generally used, among which we mention Hubbard-corrected DFT based on LSDA or σ -GGA (so-called LSDA+ U and GGA+ U [12–14] and its extensions LSDA+ U + V and GGA+ U + V [15–17] — in the following we refer to these broadly as DFT+ U and DFT+ U + V), meta-GGA functionals such as SCAN [18] (and its flavors [19,20]) and SCAN+ U [21–24], DFT with hybrid functionals (e.g., PBE0 [25] and HSE06 [26,27]), to name a few. In DFT+ U , the Hubbard U correction is applied selectively only to the partially filled d states of TM elements to alleviate SIEs for these states [28], while all other states are treated at the level of LSDA or σ -GGA. In contrast, in meta-GGA functionals the kinetic energy density is taken into account and known exact constraints are satisfied (17 in the case of SCAN). Finally, in hybrid functionals a fraction of Fock exchange is added (25% in the cases of PBE0 and HSE06) and the remainder of exchange is treated at the σ -GGA level, together with 100% of the σ -GGA correlation. In the context of a first-principle prediction of the properties of cathode materials, it still remains to establish which of these classes of advanced functionals provides the most accurate, reliable, and computationally affordable results.

The major interest in the use of Hubbard-corrected DFT comes from its ability to greatly improve the accuracy of standard DFT with only a marginal increment in the computational cost [29]. However, this is true only if the proper values of the Hubbard parameters are employed. In practice, these are unknown *a priori* and need to be determined by means of a robust protocol. One strategy that is widespread is to assign *bona fide* empirical values to the Hubbard parameters. For example, DFT + U with U parameters fitted to experimental binary metal formation energies [30] using the Kubaschewski tables [31] have proven to be effective for high-throughput search of novel cathode materials [32–35]. Also, U parameters are often calibrated empirically so that DFT+ U calculations reproduce some properties of interest (e.g., band gaps, magnetic moments, lattice parameters, oxidation enthalpies; see, e.g., Refs. [36–38]), and are used to predict other

properties (e.g., voltages, formation energies, migration barriers, etc.). If, on the one hand, experimental results might not be available for the Hubbard parameters to be fitted on, on the other hand, the so-tuned U values are not always guaranteed to be suitable for accurate predictions of other properties. Hence, finding empirically a global U parameter that makes accurate predictions on many properties of a given material at the same time is a nontrivial task. In this respect, an alternative and very attractive approach is to compute these parameters using first-principle methods [39], such as constrained DFT (cDFT) [40–48], Hartree-Fock-based approaches [16, 17, 49–52], and the constrained random phase approximation (cRPA) [53–56]. A linear-response (LR) formulation [57] of cDFT (LR cDFT) has become a method of choice for many computational Hubbard-corrected DFT studies [58,59]; moreover, its recent reformulation in terms of density-functional perturbation theory (DFPT) [60,61] further boosted its success thanks to the fact that it allows one to replace computationally expensive supercells by a primitive cell with monochromatic perturbations, thus significantly reducing the computational burden of determining the Hubbard parameters. DFT+ U with Hubbard U computed using LR cDFT [48,62–64] or cRPA [65] has proven to be effective in improving intercalation voltages and electronic structure properties of cathode materials, and, remarkably, DFT+ U + V with U and V determined from LR cDFT in a self-consistent fashion [61] was shown to provide excellent agreement with experimental voltages for olivine-type cathode materials [58], thereby highlighting the importance of intersite V Hubbard interactions. Finally, Hubbard-corrected DFT calculations are sometimes performed including van der Waals (vdW) corrections (especially for layered materials) that were shown to further improve the accuracy of the computed properties [66].

The meta-GGA SCAN functional has gained a lot of interest since its introduction in 2015 [18], in particular for modeling of cathode materials. However, it is important to note that, despite being very successful for a broad class of materials and properties, SCAN still contains significant SIEs especially when applied to TM compounds [67,68], it exhibits some potential limitations in describing magnetic systems [69,70], and it suffers from strong numerical instabilities [71]. Moreover, from a technical point of view, there are currently only few SCAN-based pseudopotentials (PPs) [72] and often GGA-based PPs are used; this inconsistency is known to introduce noticeable errors in calculating some properties of materials as, e.g., phase transition energies [73]. Nonetheless, recent applications of SCAN have shown that it gives improved descriptions of electronic properties and voltages in layered cathode materials compared to other functionals [74]; however, SCAN does not eliminate the need of the Hubbard U correction in olivine and spinel materials [75]. In

fact, SCAN with the Hubbard U correction (SCAN+ U) was shown to give more accurate predictions for many transition-metal compounds than SCAN [21–24]. In addition, SCAN and SCAN+ U are also used including the vdW corrections [75–78]; at present, only SCAN+rVV10+ U is used since the revised Vydrov-Van Voorhis (rVV10) functional [79,80] is the only vdW functional that has been parametrized for SCAN so far [81].

Finally, hybrid functionals exhibit a similar accuracy improvement over standard DFT as they work in the same direction of reducing SIEs for TM compounds [82]. At variance with Hubbard functionals and SCAN, however, their use comes at a much higher computational cost than standard DFT. Furthermore, for hybrid functionals, quite often the required fraction of Fock exchange must be tuned in solids in order to reach improved agreement with experiments [83]. This approach is no less arbitrary than picking a U value empirically. Although there are ways to determine the optimal amount of Fock exchange *ab initio* needed for each system of interest [84–89], very often the use of a tuned hybrid functional tends to deviate considerably from a pure first-principle-based practice. If one disregards the option of tuning the amount of Fock exchange, it remains the possibility to choose the hybrid functional upon considerations of its reliability for the problem of interest. In particular, for the study of cathode materials, HSE06 has proven its ability to predict accurate electronic and electrochemical properties of some paradigmatic examples of such systems as, e.g., the phospho-olivine Li_xMnPO_4 [90] and the spinel $\text{Li}_x\text{Mn}_2\text{O}_4$ [91]. The possibility to use hybrids with vdW corrections guarantees their applicability for the study of layered and organic systems [92,93].

In this paper, we present a detailed comparative study for selected olivine-type cathode materials: Li_xFePO_4 , Li_xMnPO_4 , as well as the more complex mixed-TM compound $\text{Li}_x\text{Mn}_{1/2}\text{Fe}_{1/2}\text{PO}_4$ ($x = 0, 1/4, 1/2, 3/4, 1$). We perform calculations with the four electronic-structure methods DFT, DFT+ U , DFT+ $U+V$, and HSE06, with the aim to assess the reliability of their predictions (e.g., oxidation states and Li intercalation voltages) in comparison with experiments. We show that DFT+ $U+V$ remarkably outperforms the other three well-established methods. A key requirement is that the onsite U and intersite V Hubbard parameters are determined from first-principles self-consistently using DFPT [60,61]. In particular, we demonstrate that DFT+ $U+V$ accurately predicts the electronic structure not only for the fully delithiated and lithiated compounds ($x = 0, 1$), but also for the intermediate Li concentrations ($x = 1/4, 1/2, 3/4$). Overall, HSE06 and DFT+ U results are in good qualitative agreement with DFT+ $U+V$, and superior to standard DFT, but intercalation voltages do not match the quantitative accuracy shown by DFT+ $U+V$. Importantly, DFT+ $U+V$ predicts a “digital” change in atomic occupations when gradually

changing the Li concentration, while DFT averages out the occupations over sites and HSE06 shows a less clear pattern in the “digital” change of occupations for Fe-containing phospho-olivines. This study shows that the inclusion of intersite interactions V is essential for the accurate prediction of thermodynamic quantities when electronic localization occurs in the presence of significant interatomic hybridization, confirming and enriching the findings of earlier work by some of us [58].

The paper is organized as follows. Section II presents the theoretical framework with the basics of HSE06, DFT+ U , and DFT+ $U+V$, and the linear-response calculations of U and V using DFPT. In Sec. III we present our findings for the oxidation states, Löwdin occupations, spin-resolved projected density of states (PDOS), and voltages; and in Sec. IV we provide the conclusions.

II. METHODS

In this section we discuss the basics of HSE06 [26, 27], DFT+ U [12,14], and DFT+ $U+V$ [15,29] as well as the main idea of the DFPT approach for computing Hubbard parameters [60,61]. In the following, we use the generic name “DFT + Hubbard” as broadly referring to any flavor of Hubbard-corrected DFT, which in this paper covers DFT+ U and DFT+ $U+V$. For the sake of simplicity, the formalism is presented in the framework of norm-conserving (NC) PPs in the collinear spin-polarized case. Hartree atomic units are used throughout.

A. DFT+Hubbard

For the sake of generality, here we discuss the DFT+ $U+V$ formalism [15]. It can be easily simplified to DFT+ U by setting $V = 0$. In DFT+ $U+V$, the XC energy contains a (semi)local functional (e.g., Perdew-Burke-Ernzerhof functional optimized for solids (PBEsol) [94]) and a corrective Hubbard term [15]:

$$E_{\text{XC}}^{\text{PBEsol}+U+V} = E_{\text{XC}}^{\text{PBEsol}} + E_{\text{XC}}^{U+V}. \quad (1)$$

Here E_{XC}^{U+V} is the Hubbard energy that removes (from the Hubbard manifold) SIEs present due to the use of approximations in the XC functional. At variance with the DFT+ U approach whose Hubbard corrective term only contains onsite interactions (scaled by U), DFT+ $U+V$ also features intersite interactions (scaled by V) between orbitals centered on different sites. In the simplified rotationally invariant formulation, the extended Hubbard term E_{XC}^{U+V} is defined such that it removes the mean-field PBEsol-based interactions in the Hubbard manifold and adds those that restore the piecewise linear energy behavior [29], and it

reads [15]

$$E_{\text{XC}}^{U+V} = \frac{1}{2} \sum_I \sum_{\sigma mm'} U^I (\delta_{mm'} - n_{mm'}^{II\sigma}) n_{m'm}^{II\sigma} - \frac{1}{2} \sum_I \sum_{J(J \neq I)}^* \sum_{\sigma mm'} V^{IJ} n_{mm'}^{IJ\sigma} n_{m'm}^{II\sigma}, \quad (2)$$

where σ is the spin index, I and J are atomic site indices, m and m' are the magnetic quantum numbers associated with a specific angular momentum, U^I and V^{IJ} are the effective onsite and intersite Hubbard parameters, and the asterisk in the sum denotes that, for each atom I , the index J covers all its neighbors up to a given distance (or up to a given shell). As apparent from its expression, by subtracting a term quadratic in the atomic occupations and substituting it with a linear one, the Hubbard correction contributes to decreasing the curvature of the energy as a function of the occupations of the Hubbard manifold (a measure of the effective self-interaction) and to reestablishing a piecewise linear behavior [29]. While such piecewise linearity is not a formal requirement of energy functionals, it has been long argued [28,57,95,96] that it is an essential condition to reduce SIEs in systems with very localized (e.g., d and f) electrons. The generalized occupation matrices $n_{mm'}^{IJ\sigma}$ are based on a projection of the Kohn-Sham (KS) wave functions $\psi_{v,\mathbf{k}}^\sigma(\mathbf{r})$ on localized orbitals $\varphi_m^I(\mathbf{r})$ of neighbor atoms [15]:

$$n_{mm'}^{IJ\sigma} = \sum_{v,\mathbf{k}} f_{v,\mathbf{k}}^\sigma \langle \psi_{v,\mathbf{k}}^\sigma | \varphi_m^I \rangle \langle \varphi_m^I | \psi_{v,\mathbf{k}}^\sigma \rangle. \quad (3)$$

Here v is the electronic band index, \mathbf{k} indicates points in the first Brillouin zone, $f_{v,\mathbf{k}}^\sigma$ are the occupations of the KS states, and $\varphi_m^I(\mathbf{r}) \equiv \varphi_m^{\gamma(I)}(\mathbf{r} - \mathbf{R}_I)$ are localized orbitals centered on the I th atom of type $\gamma(I)$ at position \mathbf{R}_I . It is convenient to establish a shorthand notation for the onsite occupation matrix: $n_{mm'}^{I\sigma} \equiv n_{mm'}^{II\sigma}$, which is used in DFT+ U corresponding to the first line of Eq. (2). The two terms in Eq. (2) (i.e., proportional to the onsite U^I and intersite V^{IJ} couplings) counteract each other: the onsite term favors localization on atomic sites (thus suppressing hybridization with neighbors), while the intersite term favors hybridized states with components on neighbor atoms (thus suppressing the onsite localization). It is the balance between these two competing effects that determines the ground state of the system. Therefore, accurate evaluations of U^I and V^{IJ} are crucial in this respect.

In DFT+Hubbard the values of the Hubbard parameters are not known *a priori*, and hence they are often adjusted empirically such that the final results of simulations match some experimental properties of interest (e.g., band gaps, oxidation enthalpies, etc.). This procedure introduces a degree of arbitrariness (e.g., on the choice of

experimental measurements to match) and indeterminacy (there might be several sets of interaction parameters able to reproduce a limited number of experimental results) and makes DFT+Hubbard not a fully first-principles approach. Sometimes the match to experimental measurements is also questionable on conceptual grounds, e.g., when a band gap is matched, given that exact DFT would also not reproduce the experimental gap. Most importantly, it restricts the applicability of this corrective scheme only to a domain of materials for which the Hubbard parameters can be validated with experimental results and limits its use for investigating the behavior of not-yet synthesized systems. Moreover, it is often forgotten that the Hubbard U correction is applied using Hubbard projectors that can be defined in many different ways [97,98], e.g., taken from the atomic calculations used to generate the respective pseudopotentials or their orthogonalized counterparts [see Eq. (7)], and that can be constructed with different degrees of oxidation. Hence, these Hubbard projectors and the respective U parameters are not transferable and one should not consider U as a universal number for a given element or material (see the appendix in Ref. [28]). Therefore, a first-principles calculation of the Hubbard parameters is essential for quantitative reliability and thus highly desirable.

In many cases, where localization occurs on atomic states, the effect of a finite V might actually be mimicked by a smaller value of U that avoids suppressing intersite hybridization too much. However, there are cases where localization might actually occur on bonds [15], and in these cases the use of an intersite V cannot be mimicked by any small value of U that lacks the physics needed for intersite covalent bonding. Therefore, DFT+ $U+V$ where both the U and V values are computed from first principles constitutes a robust and accurate approach that describes accurately the onsite localization and intersite hybridization of electrons without any manual calibrations of Hubbard parameters.

The aforementioned LR cDFT approach allows us to compute U and V from a generalized piecewise linearity condition [15,57]. Within this framework, the Hubbard parameters are the elements of an effective interaction matrix computed as the difference between bare and screened inverse susceptibilities [57]:

$$U^I = (\chi_0^{-1} - \chi^{-1})_{II}, \quad (4)$$

$$V^{IJ} = (\chi_0^{-1} - \chi^{-1})_{IJ}. \quad (5)$$

The susceptibility matrices χ_0 and χ measure the response of atomic occupations to a shift in the potential acting on the atomic states of a specific Hubbard atom [57]: $\chi_{IJ} = \sum_{m\sigma} (dn_{mm}^{I\sigma} / d\alpha^J)$. The difference between χ_0 and χ consists in the fact that the former represents the (bare) response to the total potential (i.e., before the electronic charge density readjusts self-consistently), while

the latter represents the (total) response to the external potential [99]. In order to avoid computationally demanding supercell calculations, required within the LR cDFT approach to make the perturbation isolated, we have recently recast the LR calculation outlined above within DFPT, so that the response to isolated perturbations can be efficiently computed from the superposition of the variation of atomic occupations to monochromatic (i.e., wave-vector-specific) perturbations using primitive cells [60]:

$$\frac{dn_{mm'}^{I\sigma}}{d\alpha^J} = \frac{1}{N_{\mathbf{q}}} \sum_{\mathbf{q}} e^{i\mathbf{q}\cdot(\mathbf{R}_l - \mathbf{R}_{l'})} \Delta_{\mathbf{q}}^{s'} n_{mm'}^{s\sigma}. \quad (6)$$

Here $\Delta_{\mathbf{q}}^{s'} n_{mm'}^{s\sigma}$ is the response of the occupation matrix; $I \equiv (l, s)$ and $J \equiv (l', s')$, where s and s' are the atomic indices in unit cells while l and l' are the unit-cell indices; \mathbf{R}_l and $\mathbf{R}_{l'}$ are the Bravais lattice vectors; and the grid of \mathbf{q} points is chosen fine enough to make the resulting atomic perturbations effectively decoupled from their periodic replicas. An exhaustive illustration of this approach can be found in Refs. [60,61], where a recent extension to ultrasoft pseudopotentials and to the projector-augmented-wave method is also discussed.

It is crucial to keep in mind that the values of the computed Hubbard parameters strongly depend on the type of Hubbard projector functions $\phi_m^I(\mathbf{r})$ that are used in DFT+Hubbard [28,97,98,100,101]. Here we employ orthogonalized atomic orbitals that are computed using the Löwdin orthogonalization method [102,103]:

$$\phi_m^I(\mathbf{r}) = \sum_{Jm'} (\hat{O}^{-1/2})_{m'm}^{JI} \phi_{m'}^J(\mathbf{r}). \quad (7)$$

Here \hat{O} is the orbital overlap matrix, whose matrix elements are defined as $(\hat{O})_{mm'}^{IJ} = \langle \phi_m^I | \phi_{m'}^J \rangle$, and $\phi_m^I(\mathbf{r})$ are the nonorthogonalized atomic orbitals provided with PPs. With this choice of projector functions, the electrons in the intersite overlap regions are not counted twice when computing the atomic occupations used in the Hubbard correction, as is the case for the nonorthogonalized atomic orbitals $\phi_m^I(\mathbf{r})$. As a matter of fact, DFT+Hubbard with the Löwdin orthogonalized orbitals has proven to give more accurate results for various properties of materials [104–110], provided the Hubbard parameters are consistently computed with the Löwdin orthogonalized orbitals. Therefore, Hubbard parameters and Hubbard projectors should always be defined consistently and reported together.

B. HSE06

In the range-separated hybrid functional HSE06 the exchange energy is divided into a short-range (S) and a long-range (L) part. Only 25% of the short-range part consists of the Fock energy and the remaining 75% is the

PBE exchange energy, while the long-range exchange part is fully computed at the PBE level [26,27]. The total XC energy is

$$E_{\text{XC}}^{\text{HSE06}} = \frac{1}{4} E_x^{\text{Fock,S}} + \frac{3}{4} E_x^{\text{PBE,S}} + E_x^{\text{PBE,L}} + E_c^{\text{PBE}}, \quad (8)$$

where E_c^{PBE} is the PBE correlation energy. The Fock short-range energy is the most computationally expensive term and it is defined by generalizing the definition of Fock [111] as

$$E_x^{\text{Fock,S}} = -\frac{1}{2} \sum_{\sigma} \sum_{v,\mathbf{k}} \sum_{v',\mathbf{k}'} \int \int d\mathbf{r} d\mathbf{r}' \text{erfc}(\omega|\mathbf{r} - \mathbf{r}'|) \times \frac{\psi_{v,\mathbf{k}}^{\sigma*}(\mathbf{r}) \psi_{v',\mathbf{k}'}^{\sigma}(\mathbf{r}) \psi_{v',\mathbf{k}'}^{\sigma*}(\mathbf{r}') \psi_{v,\mathbf{k}}^{\sigma}(\mathbf{r}')}{|\mathbf{r} - \mathbf{r}'|}, \quad (9)$$

where erfc is the complementary error function, $\omega = 0.106 a_0^{-1}$ is the screening parameter with a_0 being the Bohr radius [27]. The Fock short-range energy of Eq. (9) contains only exchange interactions at relatively short atomic length scales, and it can be assimilated to a sort of “onsite exchange” and “intersite exchange” energy contributions: the former refers to exchange acting between orbitals centered on the same atom, while the latter refers to exchange acting between orbitals centered on different atoms [91]. This aspect is crucial and in the following we further investigate such an analogy between HSE06 and DFT+Hubbard.

C. HSE06 versus DFT+Hubbard

It is instructive to establish analogies between the hybrid functional HSE06 and DFT+Hubbard [112]. It has been shown in Refs. [16,17] that DFT+ $U+V$ predicts the electronic structure of TM compounds and light-element compounds in closer agreement with HSE06 with respect to DFT+ U . However, the origin of this improvement was not investigated in detail. As will be shown in what follows, DFT+ $U+V$ is as accurate as (and occasionally better than) HSE06 in predicting electronic properties and voltages in phospho-olivines, and we provide a simple qualitative explanation for this.

DFT+ U and hybrid functionals share one important feature: they both attempt to correct SIEs for orbitals centered on the same site. However, in contrast to HSE06, DFT+ U does not correct for SIEs originating from the interactions of orbitals centered on different (neighboring) sites. This is why for systems with strong covalent bonding DFT+ U typically disagrees with HSE06 predictions. In contrast, this latter effect is captured by DFT+ $U+V$, which makes it more general and allows us to cover similar physics as that described by HSE06. However, it is important to recall that in DFT+ $U+V$ only a subset of orbitals are corrected, while hybrid functionals act on all the orbitals. Moreover,

since typically only nearest-neighbor intersite interactions are taken into account in DFT+ $U+V$, this looks similar to HSE06 that has only the short-range Fock exchange, while long-range effects are fully disregarded both in DFT+ $U+V$ and HSE06.

D. Crystal structure, magnetic ordering, and further details of calculations

The phospho-olivines Li_xFePO_4 , Li_xMnPO_4 , and $\text{Li}_x\text{Mn}_{1/2}\text{Fe}_{1/2}\text{PO}_4$ have an orthorhombic crystal structure at $x = 0$ and $x = 1$ with a $Pnma$ space group [113–115]. The unit cell contains four formula units, i.e., 24 atoms for $x = 0$ and 28 atoms for $x = 1$. The crystal structure of these systems is shown in Fig. 1 for $x = 1$. The TM atoms (labeled as M with an index from 1 to 4 in Fig. 1) are coordinated by six O atoms forming a MO_6 octahedron of which it occupies the center. The P atoms are instead at the center of PO_4 tetrahedra that they form with neighboring oxygens. The three-dimensional structure of the crystal can be understood as being based on a network of corner-sharing MO_6 octahedra further linked by “interstitial” PO_4 tetrahedra that act as structural reinforcer [avoiding excessive volume variations upon Li (de)intercalation] and chemical stabilizers (useful to avoid oxygen escapes). Li ions reside within octahedral channels parallel to the intermediate-length side of the cell.

The phospho-olivines are known to show an antiferromagnetic behavior below their transition temperatures [116–119]. In the previous study (Ref. [58]) it was shown that different antiferromagnetic arrangements of spins result in total energies that differ not more than by about

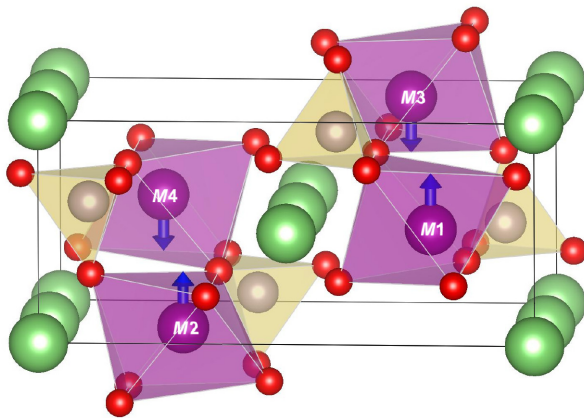


FIG. 1. Crystal structure of phospho-olivines. Transition-metal elements ($M1$ – $M4$) are indicated in purple, O atoms in red, Li atoms in green, and P atoms in yellow. Blue vertical arrows indicate the orientation of spin. In Li_xMnPO_4 , $M1$ – $M4$ correspond to Mn1–Mn4, in Li_xFePO_4 , $M1$ – $M4$ correspond to Fe1–Fe4, and in $\text{Li}_x\text{Mn}_{1/2}\text{Fe}_{1/2}\text{PO}_4$, $M1 = \text{Fe}1$, $M2 = \text{Mn}2$, $M3 = \text{Fe}3$, $M4 = \text{Mn}4$. Rendered using VESTA [120].

20 meV at the DFT+Hubbard level of theory (largely irrelevant for the calculation of voltages). In this paper we use the magnetic configuration that minimizes the total energy (labeled “ AF_1 ” in Ref. [58]), and it is depicted in Fig. 1. Moreover, we use the same spin arrangement in the mixed TM phospho-olivine $\text{Li}_x\text{Mn}_{1/2}\text{Fe}_{1/2}\text{PO}_4$. Finally, there are several configurations for arranging two Mn and two Fe atoms in the unit cell of $\text{Li}_x\text{Mn}_{1/2}\text{Fe}_{1/2}\text{PO}_4$. Our goal here is not to investigate all configurations but rather to choose one as a representative case for comparing results obtained using different approaches. To this end, we choose to arrange Mn and Fe atoms such that two Mn atoms are antiferromagnetically coupled to each other and the same for Fe atoms, as shown in Fig. 1.

All technical details of the calculations are described in Sec. S1 of the Supplemental Material [121]. Hubbard parameters are computed self-consistently using DFPT as described in Sec. II, and their values are listed in Sec. S2 of the Supplemental Material [121]. The crystal structure is optimized using DFT and DFT+Hubbard, and the results are reported in Sec. S3 of the Supplemental Material [121]; for HSE06 calculations, we use the DFT+ $U+V$ geometry since the structural optimization at the HSE06 level is computationally too expensive. The configurations for partially delithiated structures and the formation energies are discussed in Sec. S4 of the Supplemental Material [121]. Other properties reported in the Supplemental Material will be mentioned in Sec. III.

III. RESULTS AND DISCUSSION

A. Oxidation states, Löwdin occupations, and magnetic moments

The concept of oxidation state (OS) is central and ubiquitous in chemistry and physics; it is widely used to describe redox reactions, electrolysis, and many electrochemical processes as it allows one to track electron movement during reactions [123]. The main idea is that the variations in the electron number must be integer and this assigns the OS of an ion [124].

However, OS has long eluded a proper quantum-mechanical interpretation. Numerous methods have been proposed to determine the OS, and such methods often infer the OS of ions from schemes for allocating charges to ions. These schemes can be classified into categories, among which we mention: (i) partition of space with integration of the total charge density within space allocated to each ion (e.g., Bader [125] and Voronoi [126] charges), and (ii) projection of the electronic wave functions onto a localized basis (e.g., Mulliken [127] and Löwdin [102] charges, or natural bond orbitals [128]). On the one hand, in the partition schemes all orbitals contribute to the charge within the allocated volume (e.g., a sphere of a certain radius centered on an ion), thus losing the connection to the OS of individual ions and its certain manifold (e.g.,

d orbitals of TM elements). On the other hand, projection schemes present a dependence on the type of projector functions that are used to construct the localized basis set (and dependence on the cutoff radii used in some methods). The electronic populations computed using these methods are quite useful to give an indication of the OS; however, these populations are often noninteger and their changes during redox reactions are significantly smaller than the changes in the nominal electron numbers for the end elements of the reaction. Raebiger *et al.* [129] pointed out that the net physical charge belonging to a TM atom is essentially independent of its OS and that this is due to the negative-feedback charge regulation mechanism that is inherent to TM compounds [130,131]. The difficulty in accurate and unambiguous determination of the OS of ions has inspired the development of novel methods. Among these, we highlight the method of Ref. [132] that is based on wave-function topology and the modern theory of polarization, and the method of Ref. [122] that is a projection-based method that uses eigenvalues of the atomic occupation matrix to determine the OS. Whereas the OS as defined in Ref. [132] has proven to be effective for transport processes [133], here we choose to adopt the method of Ref. [122] that is particularly well suited for the purpose of the present work. In Sec. S5 in the Supplemental Material [121] we also discuss the determination of OS based on magnetic moments computed by integrating the

difference between the spin-up and spin-down components of the spin-charge density over atomic spheres of varying radius centered on ions [134].

Table I reports the population analysis data for the $3d$ shells of Mn and Fe ions in Li_xMnPO_4 and Li_xFePO_4 at $x = 0$ and $x = 1$ computed using four approaches (DFT, DFT+ U , DFT+ $U+V$, and HSE06) in comparison with the occupations that can be inferred from the nominal oxidation state of the same ion. More specifically, it shows the eigenvalues of the site-diagonal ($I = J$) atomic occupation matrix $n_{mm'}^{\uparrow\sigma}$ of size 5×5 [see Eq. (3)] in the spin-up ($\sigma = \uparrow$: λ_i^\uparrow) and spin-down ($\sigma = \downarrow$: λ_i^\downarrow) channels, Löwdin occupations $n = \sum_{i=1}^5 (\lambda_i^\uparrow + \lambda_i^\downarrow)$, magnetic moments $m = \sum_{i=1}^5 (\lambda_i^\uparrow - \lambda_i^\downarrow)$, and the OS determined using the method of Ref. [122]. The same analysis has been performed for $\text{Li}_x\text{Mn}_{1/2}\text{Fe}_{1/2}\text{PO}_4$ at $x = 0$ and 1 and is discussed in Sec. S6 in the Supplemental Material [121]; we do not show these results here since they are similar to those presented in Table I. As can be seen from the eigenvalues in Table I, the charge allocated on the $3d$ shell of TM ions (Fe and Mn) contains contributions from both the fully occupied d orbitals (i.e., the eigenvalues that are close to 1.0 [135] and are shown in bold) and nominally empty ones that, hybridizing with O- $2p$ states, give rise to fractional occupations. According to Ref. [122], in order to determine the OS, we need to count how many d states are “fully

TABLE I. Population analysis data for the $3d$ shells of Mn and Fe atoms in Li_xMnPO_4 and Li_xFePO_4 at $x = 0$ and $x = 1$ computed using DFT (PBEsol functional), DFT+ U , DFT+ $U+V$, HSE06, and the nominal data. This table shows the eigenvalues of the site-diagonal occupation matrix for the spin-up (λ_i^\uparrow , $i = \overline{1, 5}$) and spin-down (λ_i^\downarrow , $i = \overline{1, 5}$) channels, Löwdin occupations $n = \sum_i (\lambda_i^\uparrow + \lambda_i^\downarrow)$, magnetic moments $m = \sum_i (\lambda_i^\uparrow - \lambda_i^\downarrow)$, and the oxidation state (OS). For the sake of simplicity, we drop the atomic site index I from all quantities reported here. The eigenvalues are written in ascending order (from left to right) for each spin channel. The eigenvalues written in bold correspond to fully occupied states and are thus taken into account when determining the OS according to Ref. [122].

| Material | Method | x | λ_1^\uparrow | λ_2^\uparrow | λ_3^\uparrow | λ_4^\uparrow | λ_5^\uparrow | λ_1^\downarrow | λ_2^\downarrow | λ_3^\downarrow | λ_4^\downarrow | λ_5^\downarrow | n | m (μ_B) | OS |
|----------------------------|------------|-----|----------------------|----------------------|----------------------|----------------------|----------------------|------------------------|------------------------|------------------------|------------------------|------------------------|------|-----------------|----|
| Li_xMnPO_4 | DFT | 0 | 0.42 | 0.98 | 0.99 | 0.99 | 0.99 | 0.09 | 0.10 | 0.13 | 0.16 | 0.27 | 5.12 | 3.63 | +3 |
| | | 1 | 0.99 | 0.99 | 0.99 | 1.00 | 1.00 | 0.03 | 0.04 | 0.05 | 0.10 | 0.11 | 5.28 | 4.62 | +2 |
| | DFT+ U | 0 | 0.54 | 0.99 | 0.99 | 1.00 | 1.00 | 0.04 | 0.05 | 0.06 | 0.08 | 0.19 | 4.95 | 4.10 | +3 |
| | | 1 | 0.99 | 0.99 | 1.00 | 1.00 | 1.00 | 0.02 | 0.02 | 0.03 | 0.07 | 0.08 | 5.19 | 4.76 | +2 |
| | DFT+ $U+V$ | 0 | 0.50 | 0.99 | 0.99 | 1.00 | 1.00 | 0.05 | 0.06 | 0.08 | 0.09 | 0.22 | 4.98 | 3.97 | +3 |
| | | 1 | 0.99 | 0.99 | 1.00 | 1.00 | 1.00 | 0.02 | 0.02 | 0.03 | 0.07 | 0.08 | 5.21 | 4.75 | +2 |
| | HSE06 | 0 | 0.40 | 0.99 | 0.99 | 0.99 | 0.99 | 0.06 | 0.07 | 0.09 | 0.10 | 0.23 | 4.91 | 3.83 | +3 |
| | | 1 | 0.99 | 0.99 | 1.00 | 1.00 | 1.00 | 0.02 | 0.02 | 0.03 | 0.07 | 0.08 | 5.21 | 4.75 | +2 |
| | Nominal | 0 | 0.00 | 1.00 | 1.00 | 1.00 | 1.00 | 0.00 | 0.00 | 0.00 | 0.00 | 0.00 | 4.00 | 4.00 | +3 |
| | | 1 | 1.00 | 1.00 | 1.00 | 1.00 | 1.00 | 0.00 | 0.00 | 0.00 | 0.00 | 0.00 | 5.00 | 5.00 | +2 |
| Li_xFePO_4 | DFT | 0 | 0.97 | 0.98 | 0.99 | 1.00 | 1.00 | 0.15 | 0.16 | 0.17 | 0.25 | 0.26 | 5.93 | 3.94 | +3 |
| | | 1 | 0.99 | 0.99 | 0.99 | 0.99 | 1.00 | 0.06 | 0.07 | 0.13 | 0.14 | 0.98 | 6.32 | 3.57 | +2 |
| | DFT+ U | 0 | 0.99 | 0.99 | 1.00 | 1.00 | 1.00 | 0.09 | 0.10 | 0.10 | 0.22 | 0.24 | 5.72 | 4.22 | +3 |
| | | 1 | 0.99 | 0.99 | 1.00 | 1.00 | 1.00 | 0.02 | 0.04 | 0.08 | 0.09 | 1.00 | 6.20 | 3.76 | +2 |
| | DFT+ $U+V$ | 0 | 0.99 | 0.99 | 1.00 | 1.00 | 1.00 | 0.09 | 0.12 | 0.12 | 0.21 | 0.25 | 5.76 | 4.18 | +3 |
| | | 1 | 0.99 | 0.99 | 1.00 | 1.00 | 1.00 | 0.03 | 0.04 | 0.09 | 0.10 | 0.99 | 6.22 | 3.74 | +2 |
| | HSE06 | 0 | 0.99 | 0.99 | 0.99 | 0.99 | 1.00 | 0.09 | 0.10 | 0.10 | 0.19 | 0.23 | 5.67 | 4.26 | +3 |
| | | 1 | 0.99 | 0.99 | 1.00 | 1.00 | 1.00 | 0.03 | 0.04 | 0.09 | 0.09 | 0.99 | 6.22 | 3.74 | +2 |
| | Nominal | 0 | 1.00 | 1.00 | 1.00 | 1.00 | 1.00 | 0.00 | 0.00 | 0.00 | 0.00 | 0.00 | 5.00 | 5.00 | +3 |
| | | 1 | 1.00 | 1.00 | 1.00 | 1.00 | 1.00 | 0.00 | 0.00 | 0.00 | 0.00 | 1.00 | 6.00 | 4.00 | +2 |

occupied”; by following this procedure and recalling the valence electronic configurations of TM atoms considered here (Mn, $3d^5 4s^2$, and Fe, $3d^6 4s^2$) we readily find that in the fully delithiated olivines ($x = 0$) the OSs of Mn and Fe are +3 while in the fully lithiated olivines ($x = 1$) the OSs of Mn and Fe are +2. This agrees well with the nominal OSs shown in Table I and depicted in Fig. 2. In addition we find that Mn and Fe are in a high-spin state, in agreement with experiments [118,119,136]. Different methods considered here give slightly different occupations of the formally empty d states: for instance, in LiMnPO_4 the unoccupied d state in the spin-up channel (corresponding to λ_1^\uparrow) features occupations in the range 0.40 to 0.54 due to mixing with O- $2p$ ligand states, whereas much smaller filling of all d states occurs in the spin-down channel. Therefore, a larger deviation from 0 of the eigenvalues indicates a stronger mixing of the unoccupied d orbitals with the ligand orbitals, in accordance with the prescription of Ref. [122].

Table I also contains the Löwdin occupations n and magnetic moments m , which are often used to determine the OSs of ions. However, as we discussed earlier, these are not always appropriate descriptors of the OS: due to the hybridization of the TM orbitals with the states of their ligands, it is difficult to assign the correct number of electrons to the TM ions; moreover, the number of electrons on TM orbitals undergoes smaller changes than predicted by the nominal OS during (de)lithiation due to the negative-feedback charge regulation mechanism discussed in Ref. [129]. Indeed, from Table I we can see that, e.g., for FePO_4 and LiFePO_4 , the nominal Löwdin occupations are 5.0 and 6.0, respectively, while the computational predictions on average give 5.8 and 6.2 (with DFT giving the largest deviations from the nominal occupations due to SIEs). Magnetic moments are also often used to determine the OS, but here we can see that these are also not appropriate quantities: the nominal magnetic moments for FePO_4 and LiFePO_4 are 5.0 and $4.0 \mu_B$, respectively, while the computational predictions on average give 4.2 and $3.7 \mu_B$ (again, the largest deviations from the nominal magnetic moments are those of DFT due to SIEs). It is interesting to note that DFT+ $U+V$

predicts the Löwdin occupations and magnetic moments in remarkable agreement with the HSE06 ones for LiFePO_4 , while for FePO_4 , the DFT+ U results are closer to HSE06 than the DFT+ $U+V$ ones. Similar trends are also observed for MnPO_4 and LiMnPO_4 , which suggests that the TM-ligand intersite electronic interactions are slightly stronger in the fully lithiated olivines. Nevertheless, the Löwdin occupations (and magnetic moments) are still very useful quantities for bookkeeping [129], in particular when describing the gradual (de)lithiation process, as discussed in the following.

Figure 3 shows the Löwdin occupations of the $3d$ shells of Mn and Fe atoms in Li_xMnPO_4 , Li_xFePO_4 , and $\text{Li}_x\text{Mn}_{1/2}\text{Fe}_{1/2}\text{PO}_4$ at $x = 0, 1/4, 1/2, 3/4, 1$ computed using three approaches (DFT, DFT+ $U+V$, and HSE06). Here we do not show the DFT+ U results since these are known to be less accurate than the DFT+ $U+V$ ones in olivines, e.g., for $x = 1/2$ [58]; in addition, the simultaneous convergence of the Hubbard U parameters within DFT+ U and the crystal structure in a self-consistent fashion [61] is problematic for $x = 1/4$ and $3/4$ (which requires further investigation). We stress that no convergence issues were found when using self-consistent DFT+ $U+V$. Our main goal here is to compare the accuracy of the DFT+ $U+V$ approach versus the well-established HSE06 one. In the case of Li_xMnPO_4 , we can see that DFT+ $U+V$ and HSE06 agree remarkably well and both show a “digital” change in the Löwdin occupations: adding one Li^+ ion and one electron to the cathode during the lithiation process leads to changes in the occupation from 4.98 to 5.21 (and to the corresponding change in the OS from +3 to +2; see Table I) of only one Mn ion (that accepts this extra electron) while all other Mn ions remain unchanged. This process continues when we go on with the Li intercalation until eventually all Mn ions reduce from +3 to +2. Thus, these two approaches successfully describe the mixed-valence nature of the Li_xMnPO_4 compound that contains two types of Mn ions, Mn^{3+} and Mn^{2+} , at $x = 1/4, 1/2, 3/4$. In contrast, DFT fails to localize an extra electron on one of the Mn ions and, as a consequence, the charge density is spread out and equally distributed among all Mn ions in the system with

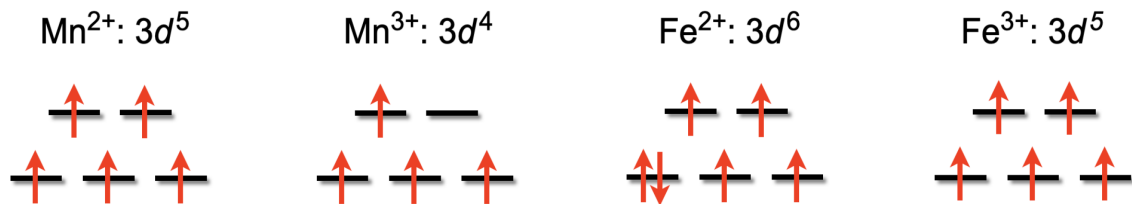


FIG. 2. Nominal occupations of the $3d$ manifolds of Mn and Fe atoms (not hybridized with ligands) in a high-spin undistorted octahedral complex with different oxidation states (O_h point group). The t_{2g} and e_g levels are indicated with black horizontal lines and are nondegenerate due to the crystal-field splitting; up and down red arrows correspond to spin-up and spin-down electrons, respectively.

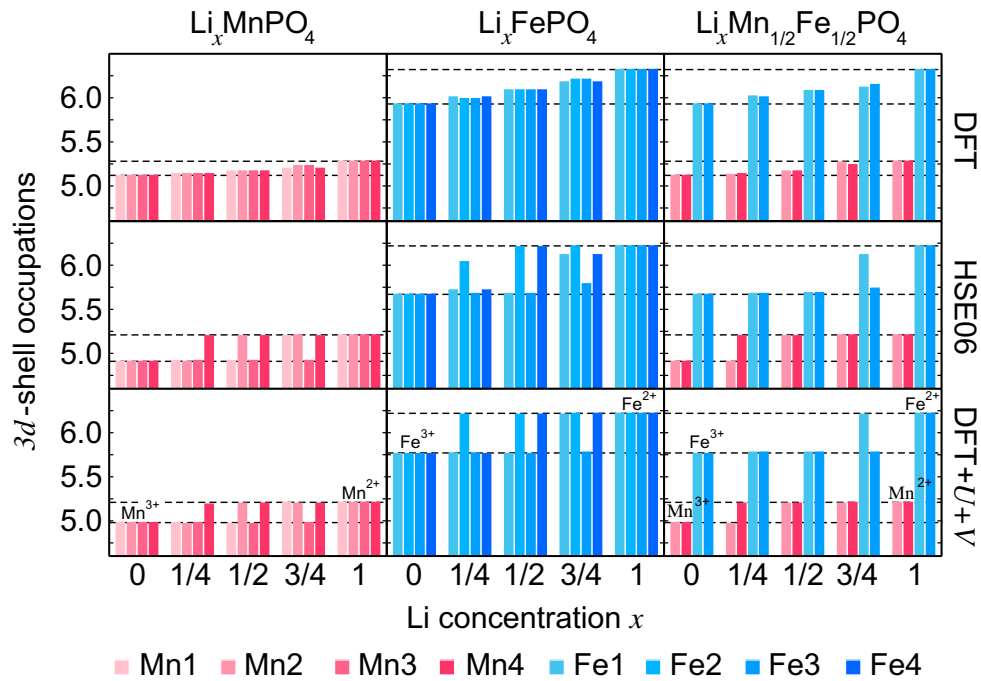


FIG. 3. Löwdin occupations of the $3d$ shells of Mn and Fe atoms in Li_xMnPO_4 , Li_xFePO_4 , and $\text{Li}_x\text{Mn}_{1/2}\text{Fe}_{1/2}\text{PO}_4$ at $x = 0, 1/4, 1/2, 3/4, 1$ computed using three approaches (DFT, DFT+ $U+V$, and HSE06). The horizontal dashed lines correspond to the Löwdin occupations of the end elements ($x = 0$ and $x = 1$) with their corresponding oxidation states determined using the data in Table I. For each material, there are four TM atoms, each of which is represented with a bar.

approximately equal occupations, as can be seen in Fig. 3. Hence, in DFT at $x = 1/4, 1/2, 3/4$ there is only one type of Mn ion whose occupations are intermediate (and progressively changing with Li content) between those of the +2 and +3 ions. In the case of Li_xFePO_4 , our results are similar with the difference that here only DFT+ $U+V$ shows the “digital” change in Löwdin occupations while HSE06 does not manage to describe accurately the localization of electrons on Fe ions. This seems to suggest that the global mixing parameter of 0.25 of HSE06 turns out to be ineffective at describing complex electronic interactions in Li_xFePO_4 , while DFT+ $U+V$ with site-dependent self-consistent Hubbard parameters U and V proves capable at capturing the local chemistry (in particular, the varying amount of $3d - 2p$ intersite hybridization) and the “digital” change in the OS of Fe ions. Finally, in $\text{Li}_x\text{Mn}_{1/2}\text{Fe}_{1/2}\text{PO}_4$ we find that Mn^{3+} ions are the first to reduce to Mn^{2+} when lithiating the compound from $x = 0$ to $x = 1/4$ and $x = 1/2$, and only at higher Li concentrations (from $x = 1/2$ to $x = 1$) Fe^{3+} ions reduce to Fe^{2+} . Importantly, we find that both DFT+ $U+V$ and HSE06 agree to describe the change in the Löwdin occupations on Mn ions, while for Fe ions, we again find that DFT+ $U+V$ outpaces HSE06 in terms of accuracy; in fact, the change in the occupation of Fe- $3d$ states is not as sharp as that obtained from the Hubbard correction. Similar trends are also observed for magnetic moments for

these three materials (see Sec. S5 in the Supplemental Material [121]).

B. Spin-resolved projected density of states

In this section we analyze the spin-resolved PDOS using three approaches (DFT, DFT+ $U+V$, and HSE06). In Fig. 4 we show the spin-resolved PDOS for $\text{Li}_x\text{Mn}_{1/2}\text{Fe}_{1/2}\text{PO}_4$ at different concentrations of Li ($x = 0, 1/4, 1/2, 3/4, 1$) as a representative example of phospho-olivines considered in this paper, while in Sec. S7 in the Supplemental Material [121] we show the spin-resolved PDOS for Li_xMnPO_4 and Li_xFePO_4 .

We can see from Fig. 4 that overall the PDOS computed using DFT+ $U+V$ and HSE06 agree very well qualitatively, while the PDOS computed using DFT shows significantly different trends. More specifically, due to the overdelocalization of d electrons of TM ions in DFT caused by SIEs, the Fe- $3d$ and Mn- $3d$ states are grouped around the Fermi level and the material exhibits spurious metallic character at $x = 1/4, 1/2, 3/4$. Furthermore, when increasing the concentration of Li within DFT, there are no clear trends in the changes of PDOS and there is no evidence that only one TM element changes its OS from +3 to +2 (in agreement with the population analysis of Sec. III A). Instead, the Li-donated extra electron is spread out over all Fe and Mn ions that results in approximately equal PDOS for the likewise TM elements. In contrast, both DFT+ $U+V$

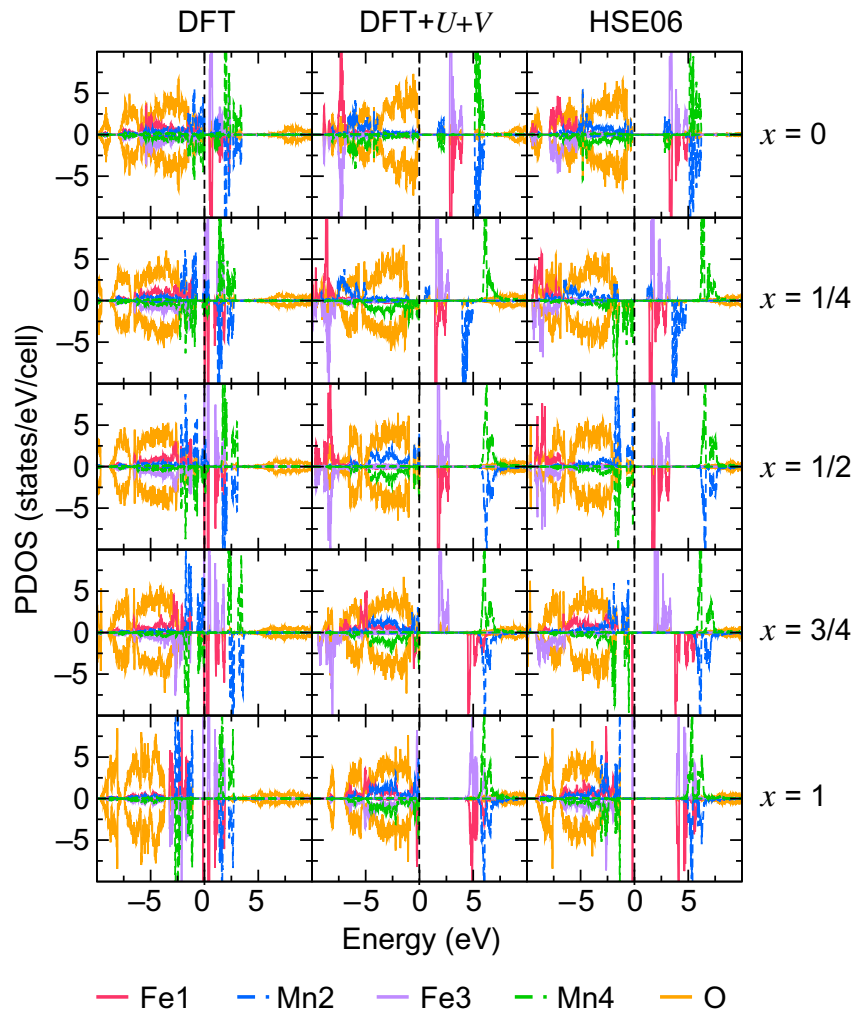


FIG. 4. Spin-resolved PDOS in $\text{Li}_x\text{Mn}_{1/2}\text{Fe}_{1/2}\text{PO}_4$ at different concentrations of Li ($x = 0, 1/4, 1/2, 3/4, 1$) for $3d$ states of Fe1, Mn2, Fe3, Mn4 and for $2p$ states of O, computed using DFT, DFT+ $U+V$, and HSE06. The PDOS for O- $2p$ states is obtained by summing contributions from all O atoms in the simulation cell and it is multiplied by a factor of 1/2 in order to have a clearer comparison with the PDOS of Fe and Mn atoms. The zero of energy corresponds to the top of the valence bands in the case of insulating ground states or the Fermi level in the case of metallic ground states. The upper part of each panel corresponds to the spin-up channel, and the lower part corresponds to the spin-down channel.

and HSE06 change drastically the PDOS compared to the DFT-based one: the material preserves its insulating character (i.e., a finite band gap) during the whole process of lithiation from $x = 0$ up to $x = 1$ (the reader is referred to Sec. S8 in the Supplemental Material [121] for the values of band gaps). When changing x from 0 to 1/4 (i.e., intercalating one Li^+ ion and adding one electron to the olivine cathode material), only the PDOS of one Mn ion (labeled “Mn4”) changes by shifting Mn- $3d$ empty states to higher energies in the spin-up channel and Mn- $3d$ occupied states closer to the top of the valence bands in the spin-down channel. Furthermore, by changing x from 1/4 to 1/2, the PDOS of the second Mn ion (labeled “Mn2”) changes in the same way as the PDOS of Mn4 but mirrored with respect to the spin channels. This is in line

with the fact that Mn is the first species to change its occupation when lithiating the structure from $x = 0$ to $x = 1/2$, as shown in Fig. 3. By further lithiating the cathode material from $x = 1/2$ to 3/4 and finally from 3/4 to 1 we can see that now the PDOS of the two Fe ions (labeled “Fe1” and “Fe3”) change by shifting Fe- $3d$ empty states to higher energies and Fe- $3d$ occupied states towards the top of the valence bands. These changes in the PDOS are consistent with the reduction of Mn^{3+} to Mn^{2+} and of Fe^{3+} to Fe^{2+} (see Sec. III A). It is interesting to note that the occupied Fe- $3d$ states are localized and show small hybridization with O- $2p$ ligand states for x in the range 0 to 1/2 (red and violet peaks at around -8 eV) while, for x from 1/2 to 1, they move up in energy, thus overlapping with the O- $2p$ states (from -7 to 0 eV) and becoming more

dispersive. This latter effect is well captured both in HSE06 and DFT+ $U+V$ since both describe the intersite electronic interactions and not only the localization of d electrons.

It is instructive to highlight the differences in the PDOS computed using DFT+ $U+V$ and HSE06. While both methods show changes in the character of the top of the valence bands when going from $x = 0$ to 1, the fine details are different. At $x = 0$, DFT+ $U+V$ shows that the top of the valence bands is strongly dominated by the O-2 p states, while HSE06 predicts that the top of the valence bands is more of a mixed nature due to the hybridization between Mn-3 d and O-2 p states. In addition, in DFT+ $U+V$ we can see a clearer energy separation between the Fe-3 d and Mn-3 d empty states at $x = 0$, while within HSE06 these states are closer in energy. At $x = 1/4$ and $x = 1/2$, both methods show that the top of the valence bands is dominated by the Mn-3 d states, although in HSE06 the intensity of these states is much stronger than in DFT+ $U+V$. Finally, at $x = 3/4$ and 1 these two methods give different predictions for the character of the top of the valence bands. In HSE06 at $x = 1$, Fe-3 d states are the highest occupied states while Mn-3 d states lie deeper in energy and there is an energy gap between these two sets of states. In contrast, in DFT+ $U+V$ at $x = 1$ there is no gap between the Fe-3 d and Mn-3 d occupied states, and all these states overlap in energy and thus the top of the valence bands is predominantly of the Fe-3 d and Mn-3 d character. To the best of our knowledge, there is no experimental data from photoemission and x-ray absorption spectroscopy measurements, so it is not possible to establish which method gives a more accurate description of the electronic structure of $\text{Li}_x\text{Mn}_{1/2}\text{Fe}_{1/2}\text{PO}_4$. However, the fact that DFT+ $U+V$ can capture the “digital” change of Löwdin occupations (especially for Fe ions) upon the lithiation of olivines (as shown in Sec. III A) suggests that the PDOS from DFT+ $U+V$ is probably more reliable than that from HSE06. Further investigations are required in order to shed more light on this issue. But the overall agreement between trends in the PDOS computed within DFT+ $U+V$ and HSE06 proves that these two methods—despite having very different mathematical formulations and theoretical background (see Sec. II)—yield on average similar predictions of the electronic structure of phospho-olivines.

C. Lithium intercalation voltages

The topotactic Li intercalation voltages can be computed using the fundamental thermodynamic definition [58,138]

$$\Phi = -\frac{E(\text{Li}_{x_2}S) - E(\text{Li}_{x_1}S) - (x_2 - x_1)E(\text{Li})}{(x_2 - x_1)e}, \quad (10)$$

where S is introduced for the sake of shorthand notation and it denotes, e.g., MnPO_4 for Li_xMnPO_4 and similarly for other cathode materials considered in this paper. Here, Φ is the voltage, e is the electronic charge, x_1 and x_2 are

the concentrations of Li and they take values between 0 and 1 in this study, and E is the total energy per formula unit. It is important to remark that $E(\text{Li})$ is the total energy of bulk Li computed at the level of standard DFT (PBEsol functional), while $E(\text{Li}_{x_1}S)$ and $E(\text{Li}_{x_2}S)$ are computed using the four approaches considered in this work: DFT, HSE06, DFT+ U , and DFT+ $U+V$ (U and V are computed self-consistently individually for each structure [58]). We note that entropic and pressure-volume effects are neglected when computing Φ since these are known to not significantly impact average Li intercalation voltages [139].

Figure 5 shows a comparison between computed voltages and experimental ones from Refs. [115,137]. For Li_xMnPO_4 and Li_xFePO_4 , we compute the average voltages in the range $0 < x < 1$ (thus $x_1 = 0$ and $x_2 = 1$) since experimentally it is known that there is only one plateau in the voltage profile [115]. In contrast, for $\text{Li}_x\text{Mn}_{1/2}\text{Fe}_{1/2}\text{PO}_4$, we compute the average voltages in two ranges of x , $0 < x < 1/2$ and $1/2 < x < 1$, which correspond to the two plateaus observed experimentally in the voltage profile [115]. As discussed in previous sections, $0 < x < 1/2$ corresponds to the reduction of Mn ions and hence the voltage is similar to that of Li_xMnPO_4 , while $1/2 < x < 1$ corresponds to the reduction of Fe ions with a voltage that is similar to that of Li_xFePO_4 . Experimentally, it is known that the mixing of TM cations creates shifts in redox potentials: the voltage of the $\text{Mn}^{2+/3+}$ couple is decreased by about 0.08 V, while the voltage of the $\text{Fe}^{2+/3+}$ couple is increased by about 0.05 V when going from the pristine end members (Li_xMnPO_4 and Li_xFePO_4) to the mixed TM olivine ($\text{Li}_x\text{Mn}_{1/2}\text{Fe}_{1/2}\text{PO}_4$) [115,137]. The shifts in redox potentials were also observed in previous (DFT+ U)-based calculations [140–142] and were attributed to changes in the TM—O bond lengths [115,137,142] or strain [141].

As can be seen from Fig. 5, standard DFT largely underestimates the voltages (on average 22%–31% off with respect to the experiments). This demonstrates that the energetics is strongly affected by the delocalization of TM d electrons due to the strong SIEs inherent to XC functionals (such as, e.g., PBEsol). HSE06 alleviates these errors partially and improves the energetics; however, the resulting voltages are overestimated by 6%–15%. It is worth noting that our HSE06-based voltages are significantly higher than those of Ref. [82] that reports 3.87 V for Li_xMnPO_4 and 3.33 V for Li_xFePO_4 using HSE06. These discrepancies are likely due to various differences in computational details (different pseudopotentials, screening parameter ω , kinetic energy cutoff, \mathbf{k} points sampling, etc.) and different geometries (here we use the DFT+ $U+V$ geometry for HSE06 calculations while in Ref. [82] the HSE06-optimized geometry was used). We recall that in HSE06 the amount of Fock exchange is fixed to 25%, and it is quite a common practice to adjust this

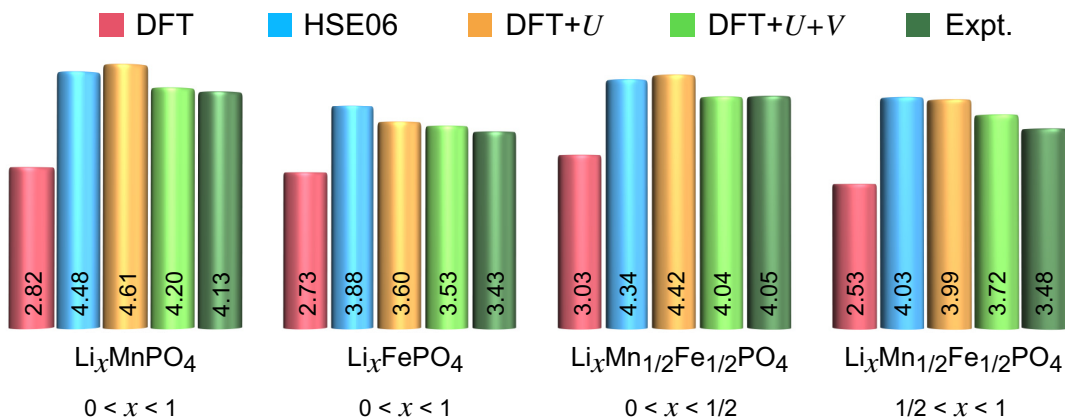


FIG. 5. Voltages versus Li/Li⁺ (in V) for Li_xMnPO₄, Li_xFePO₄, and Li_xMn_{1/2}Fe_{1/2}PO₄ computed using DFT, HSE06, DFT+*U*, and DFT+*U*+*V* with *U* and *V* determined from first principles. The experimental data are from Refs. [115,137].

percentage by reproducing, e.g., the experimental band gaps, which, as a byproduct, can lead to more accurate intercalation voltages [83]. However, the semiempirical adjustment of the amount of Fock exchange often relies on high-resolution experimental data, which are not always available.

Figure 5 shows that DFT+*U* manifests different trends with respect to HSE06 voltages depending on the material and the range of *x* considered: compared to HSE06 voltages it achieves somewhat higher values for Li_xMnPO₄, but lower ones for Li_xFePO₄ (for which voltages result closer to the experimental value). Overall, DFT+*U* voltages are scattered over a wider range (3%–14%) around the experimental values than those obtained from HSE06. It is useful to remark that our DFT+*U* voltages for Li_xMnPO₄ and Li_xFePO₄ are in better agreement with the experimental ones than those of Ref. [58]; as was pointed out in Ref. [61], this is a consequence of the difference in the values of *U*, and of the consistent calculation of forces and stresses using the orthogonalized atomic Hubbard projectors [see Eq. (7)] that has significantly refined the prediction of the equilibrium crystal structure in this work. Finally, DFT+*U*+*V* gives the most accurate predictions of voltages compared to all other methods considered in this work. More specifically, the average deviation of DFT+*U*+*V* voltages from the experimental values is in the 1%–7% range; leaving aside the Li_xMn_{1/2}Fe_{1/2}PO₄ case with 1/2 < *x* < 1, the average deviation is 1%–2%, which is remarkable given the fact that the DFT+*U*+*V* calculations are fully first-principles calculations with no fitting or adjusted parameters. This finding demonstrates that the accuracy of the DFT+*U*+*V* approach with *U* and *V* computed using linear-response theory [57,60] in a self-consistent fashion [58,61] is satisfactory for predictive simulations of olivine-type cathode materials. Regarding the redox potential shifts of the two plateaus of Li_xMn_{1/2}Fe_{1/2}PO₄ compared to Li_xMnPO₄ and Li_xFePO₄,

within DFT+*U*+*V* we find values of 0.16 and 0.19 V for the Mn^{2+/3+} and Fe^{2+/3+} couples, respectively. These redox potential shifts are similar to those obtained within HSE06, namely 0.14 and 0.15 V for the Mn^{2+/3+} and Fe^{2+/3+} couples, respectively. Therefore, both DFT+*U*+*V* and HSE06 overestimate the experimental redox potential shifts. At the same time we observe changes in the Mn—O and Fe—O bond lengths in the mixed TM olivine compared to the pristine end members (see Table S2 within the Supplemental Material [121]), in consistency with the hypothesis of Refs. [115,137,142] that these might be responsible for the redox potential shifts.

These promising results and observations motivate investigations of other classes of cathode materials using the extended Hubbard functional, and work in this direction is in progress. Furthermore, the predictive power of DFT+*U*+*V* might help to obtain further insights on still problematic aspects of the considered systems, e.g., the asymmetric charge-discharge behavior of Li_xFePO₄ possibly promoted by the existence of a hidden two-step phase transition via a metastable phase [143].

D. General remarks

In the previous sections we have shown that DFT+*U*+*V* is a powerful tool for the accurate description of the structural, electronic, magnetic, and electrochemical properties of phospho-olivines. It is useful to provide general remarks about this approach compared to state-of-the-art approaches that are currently used.

Computational cost.—DFT+*U*+*V* is only marginally more expensive than DFT+*U* when the parameters *U* and *V* are known, and both these methods are only slightly more demanding than plain DFT. However, the cost of computing *U* and *V* using DFPT is an order-of-magnitude larger (with some prefactor that depends on the number of symmetries, number of nonequivalent atoms of the same

type, etc.) than ground-state DFT calculations. Therefore, the cost of the DFT+ $U+V$ calculation itself is negligible compared to the cost of the first-principles determination of the Hubbard parameters. However, the values of U and V can be easily machine learned based on the DFPT data, as we will argue in a future publication. Compared to the computational effort associated with hybrid functionals (e.g., HSE06), that required by the self-consistent DFPT evaluation of the Hubbard parameters is still lower, especially when the number of atoms is large (greater than about ten [106]). We recall that the structural optimization using HSE06 is extremely expensive for systems containing several tens of atoms (like for phospho-olivines) and hence it was not performed in this work (although it was reported in other works, e.g., in Ref. [82]). Conversely, structural optimizations using DFT+ $U+V$ are absolutely affordable and the main cost comes from the evaluation of Hubbard forces and stresses using Löwdin-orthogonalized atomic orbitals [97,98]. We note that the structural optimization using DFT+ $U+V$ is inherently incorporated in the self-consistent protocol of the evaluation of the Hubbard parameters that brings the system to the global minimum [61]. Therefore, overall, the self-consistent DFT+ $U+V$ approach is much more affordable than HSE06 although obviously more expensive than DFT+ U with empirical U parameters.

Dependence on the availability of the experimental data.—The strength of the DFT+ $U+V$ approach used here is that it is “parameter-free” in the sense that U and V are computed from first principles without relying on any experimental data. This makes this approach predictive for novel materials for which experimental data are not available and allows us to capture the dependence of the Hubbard parameters, e.g., on the local chemical environment and on the OS. As for what concerns hybrids, when tuning the fraction of Fock exchange is necessary to improve their predictivity, an empirical strategy can also be adopted, presenting the same disadvantages as for empirically tuned Hubbard-corrected functionals. First-principles calculations of these parameters have also become increasingly popular in recent years [84–89]: however, they tend to further increase the already significant computational costs.

Generalizations and limitations.—The DFT+ $U+V$ framework is very general; it can be used with any XC functional, e.g., PBE [144], PBEsol [94], SCAN [18], rSCAN [19], r^2 SCAN [20], etc. Since SCAN and its flavors are gaining more and more popularity in the community, it would be very useful and important to generalize DFT+ $U+V$ to meta-GGAs. In practice, though, this requires, firstly, the availability of the meta-GGA pseudopotentials, and, secondly, the generalization of DFPT to meta-GGAs for a consistent evaluation of the Hubbard interactions. As for what concerns limitations, currently, our formulation of DFT+ $U+V$ does not include the

Hund’s J corrections that are known to be important in some classes of materials [145]. Moreover, DFT+ $U+V$ is a mean-field approach based on a single Slater determinant; hence, systems for which the multireference nature of the wave function is important are beyond reach for the current formulation of DFT+ $U+V$. Finally, as mentioned earlier, the simultaneous convergence of the Hubbard U parameters within DFT+ U and the crystal structure in a self-consistent fashion [61] is problematic for some fractional concentrations of Li that might be due to the missing derivatives of the Hubbard parameters with respect to atomic positions when computing Hubbard forces [146].

Data set and databases.—In the present work we consider only three examples from the same family of cathode materials (containing only two different TM ions, Mn and Fe). Therefore, our work is by no means conclusive and the accuracy of DFT+ $U+V$ for other classes of cathode materials (e.g., layered, spinel, etc.) has to be verified thoroughly and with care. However, the promising results presented in this work for phospho-olivines are very encouraging and the whole computational DFT+ $U+V$ framework is indeed very robust. Work is in progress for the development of automated DFT+ $U+V$ workflows for the high-throughput calculations for cathode materials using AiiDA [147,148], which would allow us to generate large databases of cathode materials’ properties and benchmark them versus data obtained using state-of-the-art methods and data from experiments.

IV. CONCLUSIONS

We have presented the first comparative study (using DFT, DFT+ U , DFT+ $U+V$, and HSE06) of the electronic properties and the energetics of lithium intercalation in representative phospho-olivine cathode materials: Li_xMnPO_4 , Li_xFePO_4 , and $\text{Li}_x\text{Mn}_{1/2}\text{Fe}_{1/2}\text{PO}_4$ ($x = 0, 1/4, 1/2, 3/4, 1$). In DFT+ U and DFT+ $U+V$, the Hubbard parameters U and V have been computed from first principles using density-functional perturbation theory, without any need for adjustments or *ad hoc* fitting of the model.

By determining the oxidation state of TM ions using the projection-based method of Ref. [122], we were able to analyse the change in Löwdin occupations of the d manifolds during the lithiation process. We have found that DFT fails to account for the onset of disproportionation of the TM atoms along the intermediates of the lithiation process. In contrast, DFT+ $U+V$ correctly predicts the “digital” change of Löwdin occupations upon Li intercalation (only one TM ion changes its oxidation state from +3 to +2 for each Li ion added) in all materials studied here. For comparison, HSE06 shows the “digital” change in occupations for Li_xMnPO_4 but it fails to do so for Li_xFePO_4 at $x = 1/4$ and $3/4$ and for $\text{Li}_x\text{Mn}_{1/2}\text{Fe}_{1/2}\text{PO}_4$ at $x = 3/4$. Furthermore, the investigation of the electronic

structure has revealed that both DFT+ $U+V$ and HSE06 qualitatively show similar trends in the spin-resolved projected density of states, while DFT fails dramatically due to strong self-interactions errors.

Finally, the computed intercalation voltages are greatly underestimated within DFT, whereas HSE06 brings voltages closer to the experimental values, albeit with a slight systematic overestimation. On the other hand, while DFT+ U is on average only slightly worse than HSE06, DFT+ $U+V$ outperforms HSE06 in terms of accuracy, achieving voltages in very good agreement with experiments. These findings motivate the investigation of the electrochemical properties of other classes of cathode materials (e.g., layered, spinel, etc.) using DFT+ $U+V$, and work is underway along these paths. Finally, this study paves the way for a reliable and fully first-principles design and characterization of novel cathode materials with affordable computational costs and a high level of accuracy.

ACKNOWLEDGMENTS

We acknowledge support from the Swiss National Science Foundation (SNSF), through Grant No. 200021-179138, and its National Centre of Competence in Research (NCCR) MARVEL. F.A. acknowledges the European H2020 Intersect project, Grant No. 814487. Computer time was provided by the Swiss National Supercomputing Centre (CSCS) under project No. s1073.

-
- [1] J. Goodenough and K.-S. Park, The Li-ion rechargeable battery: A perspective, *J. Am. Chem. Soc.* **135**, 1167 (2013).
- [2] G. Assat and J. Tarascon, Fundamental understanding and practical challenges of anionic redox activity in Li-ion batteries, *Nat. Energy* **3**, 373 (2018).
- [3] D. Larcher and J. Tarascon, Towards greener and more sustainable batteries for electrochemical energy storage, *Nat. Chem.* **7**, 19 (2014).
- [4] B. Kang and G. Ceder, Battery materials for ultrafast charging and discharging, *Nature* **458**, 190 (2009).
- [5] L. Monconduit, L. Croguennec, and R. Dedryvère, *Electrodes for Li-Ion Batteries*, Vol. 2 (Wiley, London, 2015).
- [6] J. Lee, A. Urban, X. Li, D. Su, G. Hautier, and G. Ceder, Unlocking the potential of cation-disordered oxides for rechargeable lithium batteries, *Science* **343**, 519 (2014).
- [7] K. Hurlbutt, S. Wheeler, I. Capone, and M. Pasta, Prussian blue analogues as cathode materials, *Joule* **2**, 1950 (2018).
- [8] P. Hohenberg and W. Kohn, Inhomogeneous electron gas, *Phys. Rev.* **136**, B864 (1964).
- [9] W. Kohn and L. Sham, Self-consistent equations including exchange and correlation effects, *Phys. Rev.* **140**, A1133 (1965).
- [10] J. Perdew and A. Zunger, Self-interaction correction to density-functional approximations for many-electron systems, *Phys. Rev. B* **23**, 5048 (1981).
- [11] P. Mori-Sánchez, A. Cohen, and W. Yang, Many-electron self-interaction error in approximate density functionals, *J. Chem. Phys.* **125**, 201102 (2006).
- [12] V. Anisimov, J. Zaanen, and O. Andersen, Band theory and Mott insulators: Hubbard U instead of Stoner I , *Phys. Rev. B* **44**, 943 (1991).
- [13] A. Liechtenstein, V. Anisimov, and J. Zaanen, Density-functional theory and strong interactions: Orbital ordering in Mott-Hubbard insulators, *Phys. Rev. B* **52**, R5467 (1995).
- [14] S. Dudarev, G. Botton, S. Savrasov, C. Humphreys, and A. Sutton, Electron-energy-loss spectra and the structural stability of nickel oxide: An LSDA+ U study, *Phys. Rev. B* **57**, 1505 (1998).
- [15] V. L. Campo Jr and M. Cococcioni, Extended DFT+ $U+V$ method with on-site and inter-site electronic interactions, *J. Phys.: Condens. Matter* **22**, 055602 (2010).
- [16] N. Tancogne-Dejean and A. Rubio, Parameter-free hybridlike functional based on an extended Hubbard model: DFT+ $U+V$, *Phys. Rev. B* **102**, 155117 (2020).
- [17] S.-H. Lee and Y.-W. Son, First-principles approach with a pseudohybrid density functional for extended Hubbard interactions, *Phys. Rev. Res.* **2**, 043410 (2020).
- [18] J. Sun, A. Ruzsinszky, and J. Perdew, Strongly Constrained and Appropriately Normed Semilocal Density Functional, *Phys. Rev. Lett.* **115**, 036402 (2015).
- [19] A. Bartók and J. Yates, Regularized SCAN functional, *J. Chem. Phys.* **150**, 161101 (2019).
- [20] J. Furness, A. Kaplan, J. Ning, J. Perdew, and J. Sun, Accurate and numerically efficient r²SCAN meta-generalized gradient approximation, *J. Phys. Chem. Lett.* **11**, 8208 (2020).
- [21] G. Gautam and E. Carter, Evaluating transition metal oxides within DFT-SCAN and SCAN+ U frameworks for solar thermochemical applications, *Phys. Rev. Mater.* **2**, 095401 (2018).
- [22] O. Long, G. Gautam, and E. Carter, Evaluating optimal U for 3d transition-metal oxides within the SCAN+ U framework, *Phys. Rev. Mater.* **4**, 045401 (2020).
- [23] J. Kaczkowski, M. Pugaczowa-Michalska, and I. Płowaś-Korus, Comparative density functional studies of pristine and doped bismuth ferrite polymorphs by GGA+ U and meta-GGA SCAN+ U , *Phys. Chem. Chem. Phys.* **23**, 8571 (2021).
- [24] N. Artrith, J. Torres, A. Urban, and M. Hybertsen, Data-driven approach to parameterize SCAN+ U for an accurate description of 3d transition metal oxide thermochemistry, *Phys. Rev. Mater.* **6**, 035003 (2022).
- [25] C. Adamo and V. Barone, Toward reliable density functional methods without adjustable parameters: The PBE0 model, *J. Chem. Phys.* **110**, 6158 (1999).
- [26] J. Heyd, G. Scuseria, and M. Ernzerhof, Hybrid functionals based on a screened Coulomb potential, *J. Chem. Phys.* **118**, 8207 (2003).
- [27] J. Heyd, G. Scuseria, and M. Ernzerhof, Erratum: "Hybrid functionals based on a screened Coulomb potential" [*J. Chem. Phys.* **118**, 8207 (2003)], *J. Chem. Phys.* **124**, 219906 (2006).

- [28] H. Kulik and N. Marzari, A self-consistent Hubbard U density-functional theory approach to the addition-elimination reactions of hydrocarbons on bare FeO^+ , *J. Chem. Phys.* **129**, 134314 (2008).
- [29] B. Himmetoglu, A. Floris, S. de Gironcoli, and M. Cococcioni, Hubbard-corrected DFT energy functionals: The LDA+ U description of correlated systems, *Int. J. Quant. Chem.* **114**, 14 (2014).
- [30] L. Wang, T. Maxisch, and G. Ceder, Oxidation energies of transition metal oxides within the GGA+ U framework, *Phys. Rev. B* **73**, 195107 (2006).
- [31] O. Kubaschewski, C. Alcock, and P. Spencer, *Thermochemical Data* (Pergamon Press: Elmsford, New York, 1993), 6th ed.
- [32] G. Hautier, A. Jain, S. Ong, B. Kang, C. Moore, R. Doe, and G. Ceder, Phosphates as lithium-ion battery cathodes: An evaluation based on high-throughput *ab initio* calculations, *Chem. Mater.* **23**, 3495 (2011).
- [33] G. Hautier, A. Jain, H. Chen, C. Moore, S. Ong, and G. Ceder, Novel mixed polyanions lithium-ion battery cathode materials predicted by high-throughput *ab initio* computations, *J. Mater. Chem.* **21**, 17147 (2011).
- [34] T. Mueller, G. Hautier, A. Jain, and G. Ceder, Evaluation of favorite-structured cathode materials for lithium-ion batteries using high-throughput computing, *Chem. Mater.* **23**, 3854 (2011).
- [35] S. Ong, V. Chevrier, G. Hautier, A. Jain, C. Moore, S. Kim, X. Ma, and G. Ceder, Voltage, stability and diffusion barrier differences between sodium-ion and lithium-ion intercalation materials, *Energy Environ. Sci.* **4**, 3680 (2011).
- [36] O. Le Bacq, A. Pasturel, and O. Bengone, Impact on electronic correlations on the structural stability, magnetism, and voltage of LiCoPO_4 battery, *Phys. Rev. B* **69**, 245107 (2004).
- [37] M. Aykol and C. Wolverton, Local environment dependent GGA+ U method for accurate thermochemistry of transition metal compounds, *Phys. Rev. B* **90**, 115105 (2014).
- [38] E. Isaacs and C. Marianetti, Compositional phase stability of strongly correlated electron materials within DFT+ U , *Phys. Rev. B* **95**, 045141 (2017).
- [39] The actual values produced by each of the first-principles approaches for determining U and V may vary substantially, in addition to the intrinsic dependence on the choice of projector functions for the Hubbard manifold, pseudopotentials, oxidation state, functional, etc.
- [40] P. Dederichs, S. Blügel, R. Zeller, and H. Akai, Ground States of Constrained Systems: Application to Cerium Impurities, *Phys. Rev. Lett.* **53**, 2512 (1984).
- [41] A. McMahan, R. Martin, and S. Satpathy, Calculated effective Hamiltonian for La_2CuO_4 and solution in the impurity Anderson approximation, *Phys. Rev. B* **38**, 6650 (1988).
- [42] O. Gunnarsson, O. Andersen, O. Jepsen, and J. Zaanen, Density-functional calculation of the parameters in the Anderson model: Application to Mn in CdTe, *Phys. Rev. B* **39**, 1708 (1989).
- [43] M. Hybertsen, M. Schlüter, and N. Christensen, Calculation of Coulomb-interaction parameters for La_2CuO_4 using a constrained-density-functional approach, *Phys. Rev. B* **39**, 9028 (1989).
- [44] O. Gunnarsson, Calculation of parameters in model Hamiltonians, *Phys. Rev. B* **41**, 514 (1990).
- [45] W. Pickett, S. Erwin, and E. Ethridge, Reformulation of the LDA+ U method for a local-orbital basis, *Phys. Rev. B* **58**, 1201 (1998).
- [46] I. Solovyev and M. Imada, Screening of Coulomb interactions in transition metals, *Phys. Rev. B* **71**, 045103 (2005).
- [47] K. Nakamura, R. Arita, Y. Yoshimoto, and S. Tsuneyuki, First-principles calculation of effective onsite Coulomb interactions of 3d transition metals: Constrained local density functional approach with maximally localized Wannier functions, *Phys. Rev. B* **74**, 235113 (2006).
- [48] M. Shishkin and H. Sato, Self-consistent parametrization of DFT+ U framework using linear response approach: Application to evaluation of redox potentials of battery cathodes, *Phys. Rev. B* **93**, 085135 (2016).
- [49] N. Mosey and E. Carter, *Ab initio* evaluation of Coulomb and exchange parameters for DFT+ U calculations, *Phys. Rev. B* **76**, 155123 (2007).
- [50] N. Mosey, P. Liao, and E. Carter, Rotationally invariant *ab initio* evaluation of Coulomb and exchange parameters for DFT+ U calculations, *J. Chem. Phys.* **129**, 014103 (2008).
- [51] A. Andriotis, R. Sheetz, and M. Menon, LSDA+ U method: A calculation of the U values at the Hartree-Fock level of approximation, *Phys. Rev. B* **81**, 245103 (2010).
- [52] L. Agapito, S. Curtarolo, and M. Buongiorno Nardelli, Reformulation of DFT+ U as a Pseudohybrid Hubbard Density Functional for Accelerated Materials Discovery, *Phys. Rev. X* **5**, 011006 (2015).
- [53] M. Springer and F. Aryasetiawan, Frequency-dependent screened interaction in Ni within the random-phase approximation, *Phys. Rev. B* **57**, 4364 (1998).
- [54] T. Kotani, *Ab initio* random-phase-approximation calculation of the frequency-dependent effective interaction between 3d electrons: Ni, Fe, and MnO, *J. Phys.: Condens. Matter* **12**, 2413 (2000).
- [55] F. Aryasetiawan, M. Imada, A. Georges, G. Kotliar, S. Biermann, and A. Lichtenstein, Frequency-dependent local interactions and low-energy effective models from electronic structure calculations, *Phys. Rev. B* **70**, 195104 (2004).
- [56] F. Aryasetiawan, K. Karlsson, O. Jepsen, and U. Schönberger, Calculations of Hubbard U from first-principles, *Phys. Rev. B* **74**, 125106 (2006).
- [57] M. Cococcioni and S. de Gironcoli, Linear response approach to the calculation of the effective interaction parameters in the LDA+ U method, *Phys. Rev. B* **71**, 035105 (2005).
- [58] M. Cococcioni and N. Marzari, Energetics and cathode voltages of LiMPO_4 olivines ($M = \text{Fe, Mn}$) from extended Hubbard functionals, *Phys. Rev. Mater.* **3**, 033801 (2019).
- [59] G. Moore, M. Horton, A. Ganose, M. Siron, and K. Persson, High-throughput determination of Hubbard U

- and Hund J values for transition metal oxides via linear response formalism, (2022), [ArXiv:arXiv:2201.04213](https://arxiv.org/abs/2201.04213).
- [60] I. Timrov, N. Marzari, and M. Cococcioni, Hubbard parameters from density-functional perturbation theory, *Phys. Rev. B* **98**, 085127 (2018).
- [61] I. Timrov, N. Marzari, and M. Cococcioni, Self-consistent Hubbard parameters from density-functional perturbation theory in the ultrasoft and projector-augmented wave formulations, *Phys. Rev. B* **103**, 045141 (2021).
- [62] F. Zhou, C. Marianetti, M. Cococcioni, D. Morgan, and G. Ceder, Phase separation in LiFePO_4 induced by correlation effects, *Phys. Rev. B* **69**, 201101(R) (2004).
- [63] F. Zhou, M. Cococcioni, C. Marianetti, D. Morgan, and G. Ceder, First-principles prediction of redox potentials in transition-metal compounds with LDA+ U , *Phys. Rev. B* **70**, 235121 (2004).
- [64] F. Zhou, K. Kang, T. Maxisch, G. Ceder, and D. Morgan, The electronic structure and band gap of LiFePO_4 and LiMnPO_4 , *Solid State Commun.* **132**, 181 (2004).
- [65] B. Kim, K. Kim, and S. Kim, Quantification of Coulomb interactions in layered lithium and sodium battery cathode materials, *Phys. Rev. Mater.* **5**, 035404 (2021).
- [66] M. Aykol, S. Kim, and C. Wolverton, van der Waals interactions in layered lithium cobalt oxides, *J. Phys. Chem. C* **119**, 19053 (2015).
- [67] D. A. Kitchaev, H. Peng, Y. Liu, J. Sun, J. P. Perdew, and G. Ceder, Energetics of MnO_2 polymorphs in density functional theory, *Phys. Rev. B* **93**, 045132 (2016).
- [68] Y. Hinuma, H. Hayashi, Y. Kumagai, I. Tanaka, and F. Oba, Comparison of approximations in density functional theory calculations: Energetics and structure of binary oxides, *Phys. Rev. B* **96**, 094102 (2017).
- [69] M. Ekholm, D. Gambino, H. Jönsson, F. Tasnádi, B. Alling, and I. Abrikosov, Assessing the SCAN functional for itinerant electron ferromagnets, *Phys. Rev. B* **98**, 094413 (2018).
- [70] F. Tran, G. Baudesson, J. Carrete, G. Madsen, P. Blaha, K. Schwarz, and D. Singh, Shortcomings of meta-GGA functionals when describing magnetism, *Phys. Rev. B* **102**, 024407 (2020).
- [71] S. Lehtola and M. Marques, Many recent density functionals are numerically unstable, (2022), [ArXiv:2206.14062](https://arxiv.org/abs/2206.14062).
- [72] <https://yaoyi92.github.io/scan-tm-pseudopotentials.html>.
- [73] Y. Yao and Y. Kanai, Plane-wave pseudopotential implementation and performance of SCAN meta-GGA exchange-correlation functional for extended systems, *J. Chem. Phys.* **146**, 224105 (2017).
- [74] A. Chakraborty, M. Dixit, D. Aurbach, and D. Major, Predicting accurate cathode properties of layered oxide materials using the SCAN meta-GGA density functional, *npj Comput. Mater.* **4**, 60 (2018).
- [75] E. Isaacs, S. Patel, and C. Wolverton, Prediction of Li intercalation voltages in rechargeable battery cathode materials: Effects of exchange-correlation functional, van der Waals interactions, and Hubbard U , *Phys. Rev. Mater.* **4**, 065405 (2020).
- [76] X. Zhao, Y. Tian, Z. Lun, Z. Cai, T. Chen, B. Ouyang, and G. Ceder, Design principles for zero-strain Li-ion cathodes, *Joule* **6**, 1 (2022).
- [77] H. Peng and J. Perdew, Synergy of van der Waals and self-interaction corrections in transition metal monoxides, *Phys. Rev. B* **96**, 100101(R) (2017).
- [78] O. Long, G. Gautam, and E. Carter, Assessing cathode property prediction via exchange-correlation functionals with and without long-range dispersion corrections, *Phys. Chem. Chem. Phys.* **23**, 24726 (2021).
- [79] O. Vydrov and T. Van Voorhis, Nonlocal van der Waals density functional: The simpler the better, *J. Chem. Phys.* **133**, 244103 (2010).
- [80] R. Sabatini, T. Gorni, and S. de Gironcoli, Nonlocal van der Waals density functional made simple and efficient, *Phys. Rev. B* **87**, 041108 (2013).
- [81] H. Peng, Z.-H. Yang, J. Perdew, and J. Sun, Versatile van der Waals Density Functional Based on a Meta-Generalized Gradient Approximation, *Phys. Rev. X* **6**, 041005 (2016).
- [82] V. Chevrier, S. Ong, R. Armiento, M. Chan, and G. Ceder, Hybrid density functional calculations of redox potentials and formation energies of transition metal compounds, *Phys. Rev. B* **82**, 075122 (2010).
- [83] D. Seo, A. Urban, and G. Ceder, Calibrating transition-metal energy levels and oxygen bands in first-principles calculations: Accurate prediction of redox potentials and charge transfer in lithium transition-metal oxides, *Phys. Rev. B* **92**, 115118 (2015).
- [84] J. Skone, M. Govoni, and G. Galli, Self-consistent hybrid functional for condensed systems, *Phys. Rev. B* **89**, 195112 (2014).
- [85] J. Skone, M. Govoni, and G. Galli, Nonempirical range-separated hybrid functionals for solids and molecules, *Phys. Rev. B* **93**, 235106 (2016).
- [86] T. Bischoff, J. Wiktor, W. Chen, and A. Pasquarello, Nonempirical hybrid functionals for band gaps of inorganic metal-halide perovskites, *Phys. Rev. Mater.* **3**, 123802 (2019).
- [87] L. Kronik, T. Stein, S. Refaely-Abramson, and R. Baer, Excitation gaps of finite-sized systems from optimally tuned range-separated hybrid functionals, *J. Chem. Theory Comput.* **8**, 1515 (2012).
- [88] D. Wing, G. Ohad, J. Haber, M. Filip, S. Gant, J. Neaton, and L. Kronik, Band gaps of crystalline solids from Wannier-localization based optimal tuning of a screened range-separated hybrid functional, *Proc. Natl. Acad. Sci. U. S. A.* **118**, e2104556118 (2021).
- [89] M. Lorke, P. Deák, and T. Frauenheim, Koopmans-compliant screened exchange potential with correct asymptotic behavior for semiconductors, *Phys. Rev. B* **102**, 235168 (2020).
- [90] S. Ong, V. Chevrier, and G. Ceder, Comparison of small polaron migration and phase separation in olivine LiMnPO_4 and LiFePO_4 using hybrid density functional theory, *Phys. Rev. B* **83**, 075112 (2011).
- [91] M. Eckhoff, P. Blöchl, and J. Behler, Hybrid density functional theory benchmark study on lithium manganese oxides, *Phys. Rev. B* **101**, 205113 (2020).
- [92] H. Peelaers and C. Van de Walle, First-principles study of van der Waals interactions in MoS_2 and MoO_3 , *J. Phys.: Condens. Matter* **26**, 305502 (2014).
- [93] W. Zhang, P. Sun, and S. Sun, A precise theoretical method for high-throughput screening of novel organic

- electrode materials for Li-ion batteries, *J. Materiomics* **3**, 184 (2017).
- [94] J. Perdew, A. Ruzsinszky, G. Csonka, O. Vydrov, G. Scuseria, L. Constantin, X. Zhou, and K. Burke, Restoring the Density-Gradient Expansion for Exchange in Solids and Surfaces, *Phys. Rev. Lett.* **100**, 136406 (2008).
- [95] H. Kulik, M. Cococcioni, D. Scherlis, and N. Marzari, Density Functional Theory in Transition-Metal Chemistry: A Self-Consistent Hubbard U Approach, *Phys. Rev. Lett.* **97**, 103001 (2006).
- [96] H. Kulik and N. Marzari, Transition-metal dioxides: A case for the intersite term in Hubbard-model functionals, *J. Chem. Phys.* **134**, 094103 (2011).
- [97] I. Timrov, F. Aquilante, L. Binci, M. Cococcioni, and N. Marzari, Pulay forces in density-functional theory with extended Hubbard functionals: From nonorthogonalized to orthogonalized manifolds, *Phys. Rev. B* **102**, 235159 (2020).
- [98] I. Timrov, F. Aquilante, L. Binci, M. Cococcioni, and N. Marzari, Pulay forces in density-functional theory with extended Hubbard functionals: from nonorthogonalized to orthogonalized manifolds, *Phys. Rev. B* **105**, 199901 (2022).
- [99] E. Linscott, D. Cole, M. Payne, and D. O'Regan, Role of spin in the calculation of Hubbard U and Hund's J parameters from first principles, *Phys. Rev. B* **98**, 235157 (2018).
- [100] C. Tablero, Representations of the occupation number matrix on the LDA/GGA+ U method, *J. Phys.: Condens. Matter* **20**, 325205 (2008).
- [101] Y.-C. Wang, Z.-H. Chen, and H. Jiang, The local projection in the density functional theory plus U approach: A critical assessment, *J. Chem. Phys.* **144**, 144106 (2016).
- [102] P.-O. Löwdin, On the non-orthogonality problem connected with the use of atomic wave functions in the theory of molecules and crystals, *J. Chem. Phys.* **18**, 365 (1950).
- [103] I. Mayer, On Löwdin's method of symmetric orthogonalization, *Int. J. Quant. Chem.* **90**, 63 (2002).
- [104] C. Ricca, I. Timrov, M. Cococcioni, N. Marzari, and U. Aschauer, Self-consistent DFT+ $U+V$ study of oxygen vacancies in SrTiO₃, *Phys. Rev. Res.* **2**, 023313 (2020).
- [105] I. Timrov, P. Agrawal, X. Zhang, S. Erat, R. Liu, A. Braun, M. Cococcioni, M. Calandra, N. Marzari, and D. Passerone, Electronic structure of Ni-substituted LaFeO₃ from near edge x-ray absorption fine structure experiments and first-principles simulations, *Phys. Rev. Res.* **2**, 033265 (2020).
- [106] N. Kirchner-Hall, W. Zhao, Y. Xiong, I. Timrov, and I. Dabo, Extensive benchmarking of DFT+ U calculations for predicting band gaps, *Appl. Sci.* **11**, 2395 (2021).
- [107] Y. Xiong, *et al.*, Optimizing accuracy and efficacy in data-driven materials discovery for the solar production of hydrogen, *Energy Environ. Sci.* **14**, 2335 (2021).
- [108] M. Cococcioni and A. Floris, Magnetic energy landscape of dimolybdenum tetraacetate on a bulk insulator surface, *Appl. Sci.* **11**, 3806 (2021).
- [109] R. Mahajan, I. Timrov, N. Marzari, and A. Kashyap, Importance of intersite Hubbard interactions in β -MnO₂: A first-principles DFT+ $U+V$ study, *Phys. Rev. Mater.* **5**, 104402 (2021).
- [110] R. Mahajan, A. Kashyap, and I. Timrov, Pivotal role of intersite Hubbard interactions in Fe-doped α -MnO₂, *J. Phys. Chem. C* **126**, 14353 (2022).
- [111] T. Kotani, Exact Exchange Potential Band-Structure Calculations by the Linear Muffin-Tin Orbital-Atomic-Sphere Approximation Method, *Phys. Rev. Lett.* **74**, 2989 (1995).
- [112] In Refs. [149,150] a connection between DFT+ U and GW [151] was established. Also, studies have tried to understand whether DFT+ U mimics hybrid functionals [152–155], concluding that it may or may not mimic hybrids depending on the atom, the subshell, and the property that is considered.
- [113] Z. Nie, C. Ouyang, J. Chen, Z. Zhong, Y. Du, D. Liu, S. Shi, and M. Lei, First principles study of Jahn-Teller effects in Li_xMnPO₄, *Solid State Commun.* **150**, 40 (2010).
- [114] A. Padhi, K. Nanjundaswamy, and J. Goodenough, Phospho-olivines as positive-electrode materials for rechargeable lithium batteries, *J. Electrochem. Soc.* **144**, 1188 (1997).
- [115] T. Muraliganth and A. Manthiram, Understanding the shifts in the redox potentials of olivines LiM_{1-y}M_yPO₄ (M = Fe, Mn, Co, and Mg) solid solution cathodes, *J. Phys. Chem. C* **114**, 15530 (2010).
- [116] R. Newnham, R. Santoro, and M. Redman, Neutron-diffraction study of LiMnPO₄, *J. Phys. Chem. Solids* **26**, 445 (1965).
- [117] R. Santoro and R. Newnham, Antiferromagnetism in LiFePO₄, *Acta Cryst.* **22**, 344 (1967).
- [118] G. Rousse, J. Rodriguez-Carvajal, S. Patoux, and C. Masquelier, Magnetic structures of the triphylite LiFePO₄ and of its delithiated form FePO₄, *Chem. Mater.* **15**, 4082 (2003).
- [119] S. Gnewuch and E. Rodriguez, Distinguishing the intrinsic antiferromagnetism in polycrystalline LiCoPO₄ and LiMnPO₄ olivines, *Inorg. Chem.* **59**, 5883 (2020).
- [120] K. Momma and F. Izumi, VESTA: a three-dimensional visualization system for electronic and structural analysis, *J. Appl. Crystallogr.* **41**, 653 (2008).
- [121] See Supplemental Material at <http://link.aps.org/supplemental/10.1103/PRXEnergy.1.033003> for the technical details of calculations, the values of Hubbard parameters, crystal structure parameters, formation energies, population analysis, magnetic moments, projected density of states, bands gaps, and which includes Refs. [156–183].
- [122] P. H.-L. Sit, R. Car, M. H. Cohen, and A. Selloni, Simple, unambiguous theoretical approach to oxidation state determination via first-principles calculations, *Inorg. Chem.* **50**, 10259 (2011).
- [123] C. Jorgensen, *Oxidation Numbers and Oxidation States* (Springer-Verlag, New York Inc., 1969).
- [124] <https://goldbook.iupac.org/O04365.html>.
- [125] R. Bader, *Atoms in Molecules. A Quantum Theory* (Oxford University Press, Oxford, U.K., 1990).
- [126] F. Bickelhaupt, N. van Eikema, C. Fonseca Guerra, and E. Baerends, The carbon-lithium electron pair bond in (CH₃Li)_n ($n = 1, 2, 4$), *Organometallics* **15**, 2923 (1996).

- [127] R. Mulliken, Electronic population analysis on LCAO–MO molecular wave functions. I, *J. Chem. Phys.* **23**, 1833 (1955).
- [128] A. Reed, L. Curtiss, and F. Weinhold, Intermolecular interactions from a natural bond orbital, donor-acceptor viewpoint, *Chem. Rev.* **88**, 899 (1988).
- [129] H. Raebiger, S. Lany, and A. Zunger, Charge self-regulation upon changing the oxidation state of transition metals in insulators, *Nature* **453**, 763 (2008).
- [130] R. Resta, Charge states in transition, *Nature* **453**, 735 (2008).
- [131] M. Jansen and U. Wedig, A piece of the picture – misunderstanding of chemical concepts, *Angew. Chem., Int. Ed.* **47**, 10026 (2008).
- [132] L. Jiang, S. Levchenko, and A. Rappe, Rigorous Definition of Oxidation States of Ions in Solids, *Phys. Rev. Lett.* **108**, 166403 (2012).
- [133] P. Pegolo, F. Grasselli, and S. Baroni, Oxidation States, Thouless’ Pumps, and Nontrivial Ionic Transport in Nonstoichiometric Electrolytes, *Phys. Rev. X* **10**, 041031 (2020).
- [134] J. Reed and G. Ceder, Charge, potential, and phase stability of layered $\text{Li}(\text{Ni}_{0.5}\text{Mn}_{0.5})\text{O}_2$, *Electrochem. Solid-State Lett.* **5**, A145 (2002).
- [135] Possible reasons for deviations of eigenvalues (corresponding to the fully occupied states) from unity is discussed in Ref. [122].
- [136] O. Ofer, J. Sugiyama, J. Brewer, M. Månsson, K. Prša, E. Ansaldò, G. Kobayashi, and R. Kanno, The magnetic phase of lithium transition metal phosphates LiMPO_4 ($M = \text{Mn, Co, Ni}$) detected by $\mu^+\text{SR}$, *Phys. Procedia* **30**, 160 (2012).
- [137] G. Kobayashi, A. Yamada, S.-i. Nishimura, R. Kanno, Y. Kobayashi, S. Seki, Y. Ohno, and H. Miyashiro, Shift of redox potential and kinetics in $\text{Li}_x(\text{Mn}_y\text{Fe}_{1-y})\text{PO}_4$, *J. Power Sources* **189**, 397 (2009).
- [138] M. Aydinol, A. Kohan, G. Ceder, K. Cho, and J. Joannopoulos, *Ab initio* study of lithium intercalation in metal oxides and metal dichalcogenides, *Phys. Rev. B* **56**, 1354 (1997).
- [139] M. Aydinol, A. Kohan, and G. Ceder, *Ab initio* calculation of the intercalation voltage of lithium-transition-metal oxide electrodes for rechargeable batteries, *J. Power Sources* **68**, 664 (1997).
- [140] R. Malik, F. Zhou, and G. Ceder, Phase diagram and electrochemical properties of mixed olivines from first-principles calculations, *Phys. Rev. B* **79**, 214201 (2009).
- [141] D. Snyder and C. Wolverton, Transition-metal mixing and redox potentials in $\text{Li}_x(\text{M}_{1-y}\text{M}'_y)\text{PO}_4$ ($M, M' = \text{Mn, Fe, Ni}$) olivine materials from first-principles calculations, *J. Phys. Chem. C* **120**, 5932 (2016).
- [142] S. Loftager, S. Schougaard, T. Vegge, and J. García-Lastra, Density functional theory study of redox potential shifts in $\text{Li}_x\text{Mn}_y\text{Fe}_{1-y}\text{PO}_4$ battery electrodes, *J. Phys. Chem. C* **123**, 102 (2019).
- [143] Y. Koyama, T. Uyama, Y. Orikasa, T. Naka, H. Komatsu, K. Shimoda, H. Murayama, K. Fukuda, H. Arai, E. Matsubara, Y. Uchimoto, and Z. Ogumi, Hidden two-step phase transition and competing reaction pathways in LiFePO_4 , *Chem. Mater.* **29**, 2855 (2017).
- [144] J. Perdew, K. Burke, and M. Ernzerhof, Generalized Gradient Approximation Made Simple, *Phys. Rev. Lett.* **77**, 3865 (1996).
- [145] B. Himmetoglu, R. Wentzcovitch, and M. Cococcioni, First-principles study of electronic and structural properties of CuO , *Phys. Rev. B* **84**, 115108 (2011).
- [146] H. Kulik and N. Marzari, Accurate potential energy surfaces with a DFT+ U (R) approach, *J. Chem. Phys.* **135**, 194105 (2011).
- [147] G. Pizzi, A. Cepellotti, R. Sabatini, N. Marzari, and B. Kozinsky, AiiDA: Automated interactive infrastructure and database for computational science, *Comput. Mater. Sci.* **111**, 218 (2016).
- [148] S. Huber, *et al.*, AiiDA 1.0, a scalable computational infrastructure for automated reproducible workflows and data provenance, *Sci. Data* **7**, 300 (2020).
- [149] V. Anisimov, F. Aryasetiawan, and A. Lichtenstein, First-principles calculations of the electronic structure and spectra of strongly correlated systems: The LDA+ U method, *J. Phys.: Condens. Matter* **9**, 767 (1997).
- [150] H. Jiang, R. Gomez-Abal, P. Rinke, and M. Scheffler, First-principles modeling of localized d states with the $GW@LDA+U$ approach, *Phys. Rev. B* **82**, 045108 (2010).
- [151] L. Hedin, New Method for calculating the one-particle Green’s function with application to the electron-gas problem, *Phys. Rev.* **139**, A796 (1965).
- [152] V. Iváady, R. Armiento, K. Szász, E. Janzén, A. Gali, and I. Abrikosov, Theoretical unification of hybrid-DFT and DFT+ U methods for the treatment of localized orbitals, *Phys. Rev. B* **90**, 035146 (2014).
- [153] P. Verma and D. Truhlar, Does DFT+ U mimic hybrid density functionals?, *Theor. Chem. Ac.* **135**, 182 (2016).
- [154] T. Gani and H. Kulik, Where does the density localize? Convergent behavior for global hybrids, range separation, and DFT+ U , *J. Chem. Theor. Comput.* **12**, 5931 (2016).
- [155] Q. Zhao and H. Kulik, Where does the density localize in the solid state? Divergent behavior for hybrids and DFT+ U , *J. Chem. Theor. Comput.* **14**, 670 (2018).
- [156] P. Giannozzi, *et al.*, Quantum ESPRESSO: A modular and open-source software project for quantum simulations of materials, *J. Phys.: Condens. Matter* **21**, 395502 (2009).
- [157] P. Giannozzi, *et al.*, Advanced capabilities for materials modelling with Quantum ESPRESSO, *J. Phys.: Condens. Matter* **29**, 465901 (2017).
- [158] P. Giannozzi, O. Basergio, P. Bonfà, D. Brunato, R. Car, I. Carnimeo, C. Cavazzoni, S. de Gironcoli, P. Delugas, F. Ferrari Ruffino, A. Ferretti, N. Marzari, I. Timrov, A. Urru, and S. Baroni, Quantum ESPRESSO toward the exascale, *J. Chem. Phys.* **152**, 154105 (2020).
- [159] G. Prandini, A. Marrazzo, I. E. Castelli, N. Mounet, and N. Marzari, Precision and efficiency in solid-state pseudopotential calculations, *npj Comput. Mater.* **4**, 1 (2018).
- [160] The SSSP library of the Materials Cloud: <https://www.materialscloud.org/discover/sssp/table/precision>.
- [161] K. Garrity, J. Bennett, K. Rabe, and D. Vanderbilt, Pseudopotentials for high-throughput DFT calculations, *Comput. Mater. Sci.* **81**, 446 (2014).

- [162] E. Kucukbenli, M. Monni, B. Adetunji, X. Ge, G. Adebayo, N. Marzari, S. de Gironcoli, and A. Dal Corso, Projector augmented-wave and all-electron calculations across the periodic table: A comparison of structural and energetic properties, (2014), [ArXiv:1404.3015](https://arxiv.org/abs/1404.3015).
- [163] A. Dal Corso, Pseudopotentials periodic table: from H to Pu, *Comput. Mater. Sci.* **95**, 337 (2014).
- [164] M. van Setten, M. Giantomassi, E. Bousquet, M. Verstraete, D. Hamann, X. Gonze, and G.-M. Rignanese, The PSEUDODOJO: Training and grading a 85 element optimized norm-conserving pseudopotential table, *Comput. Phys. Commun.* **226**, 39 (2018).
- [165] R. Fletcher, *Practical Methods of Optimization* (Wiley, Chichester, 1987), 2nd ed.
- [166] N. Marzari, D. Vanderbilt, A. De Vita, and M. Payne, Thermal Contraction and Disorder of the Al(110) Surface, *Phys. Rev. Lett.* **82**, 3296 (1999).
- [167] I. Timrov, N. Marzari, and M. Cococcioni, HP – A code for the calculation of Hubbard parameters using density-functional perturbation theory, *Comput. Phys. Commun.* **279**, 108455 (2022).
- [168] M. Payne, M. Teter, D. Allen, T. Arias, and J. Joannopoulos, Iterative minimization techniques for *ab initio* total-energy calculations: Molecular dynamics and conjugate gradients, *Rev. Mod. Phys.* **64**, 1045 (1992).
- [169] D. Johnson, Modified Broyden's method for accelerating convergence in self-consistent calculations, *Phys. Rev. B* **38**, 12807 (1988).
- [170] F. Gygi and A. Baldereschi, Self-consistent Hartree-Fock and screened-exchange calculations in solids: Application to silicon, *Phys. Rev. B* **34**, 4405(R) (1986).
- [171] I. Timrov, F. Aquilante, M. Cococcioni, and N. Marzari, Accurate electronic properties and intercalation voltages of olivine-type Li-ion cathode materials from extended Hubbard functionals, *Materials Cloud Archive* **2022.118**, (2022), doi: [10.24435/materialscloud:7h-7q](https://doi.org/10.24435/materialscloud:7h-7q).
- [172] A. Yamada, Y. Takei, H. Koizumi, N. Sonoyama, and R. Kanno, Electrochemical, magnetic, and structural investigation of the $\text{Li}_x(\text{Mn}_y\text{Fe}_{1-y})\text{PO}_4$ olivine phases, *Chem. Mater.* **18**, 804 (2006).
- [173] Y. Asari, Y. Suwa, and T. Hamada, Formation and diffusion of vacancy-polaron complex in olivine-type LiMnPO_4 and LiFePO_4 , *Phys. Rev. B* **84**, 134113 (2011).
- [174] D.-H. Seo, H. Gwon, S.-W. Kim, J. Kim, and K. Kang, Multicomponent olivine cathode for lithium rechargeable batteries: A first-principles study, *Chem. Mater.* **22**, 518 (2010).
- [175] M. Johannes, K. Hoang, J. Allen, and K. Gaskell, Hole polaron formation and migration in olivine phosphate materials, *Phys. Rev. B* **85**, 115106 (2012).
- [176] L. Piper, N. Quackenbush, S. Sallis, D. Scanlon, G. Watson, K.-W. Nam, X.-Q. Yang, K. Smith, F. Omenya, N. Chernova, and M. Whittingham, Elucidating the nature of pseudo Jahn-Teller distortions in Li_xMnPO_4 : Combining density functional theory with soft and hard X-ray spectroscopy, *J. Phys. Chem. C* **117**, 10383 (2013).
- [177] D. Morgan, A. Van der Ven, and G. Ceder, Li conductivity in Li_xMPO_4 ($M = \text{Mn, Fe, Co, Ni}$) olivine materials, *Electrochem. Solid-State Lett.* **7**, A30 (2004).
- [178] C. Ou-Yang, S. Shi, Z. Wang, X. Huang, and L. Chen, First-principles study of Li ion diffusion in LiFePO_4 , *Phys. Rev. B* **69**, 104303 (2004).
- [179] M. Islam, D. Driscoll, C. Fisher, and P. Slater, Atomic-scale investigation of defects, dopants, and lithium transport in the LiFePO_4 olivine-type battery material, *Chem. Mater.* **17**, 5085 (2005).
- [180] S. Nishimura, G. Kobayashi, K. Ohoyama, R. Kanno, M. Yashima, and A. Yamada, Experimental visualization of lithium diffusion in Li_xFePO_4 , *Nat. Mater.* **7**, 707 (2008).
- [181] A. Yamada, Y. Kudo, and K.-Y. Liu, Phase diagram of $\text{Li}_x(\text{Mn}_y\text{Fe}_{1-y})\text{PO}_4$ ($0 \leq x, y \leq 1$), *J. Electrochem. Soc.* **148**, A1153 (2001).
- [182] K. Zaghbi, A. Mauer, J. Goodenough, F. Gendron, and C. Julien, Electronic, optical, and magnetic properties of LiFePO_4 : Small magnetic polaron effects, *Chem. Mater.* **19**, 3740 (2007).
- [183] Y. Zhang, J. Alarco, A. Best, G. Snook, P. Talbot, and J. Nerkar, Re-evaluation of experimental measurements for the validation of electronic band structure calculations for LiFePO_4 and FePO_4 , *RSC Adv.* **9**, 1134 (2019).